

PROPOSITIONS

1. Severe cloud cover is the main reason for monitoring tropical trees with an active microwave system.
(This Thesis)
2. Use of two orthogonal interferometric SAR data acquisitions is for three-dimensional canopy reconstruction at C-band more promising than multi-baseline interferometric SAR (tomographic SAR).
(This Thesis)
3. The Gibbs Markov random field model which is frequently applied to image reconstruction problems is a physical representation in which the cause and effect relation between the basic parameters (clique potentials, system temperature) and the model output (the random field) cannot be interpreted in a straightforward way.
4. Experiment is the *sole judge* of scientific 'truth'.
(Richard P. Feynman, 1963)
5. Color visualisation methods for scientific data may lead to misinterpretation of spatial patterns when human visual perception is not accounted for in the mapping from data value to displayed color.
6. Helium and sun powered airships should be considered as candidates for solving current constipation of the Dutch traffic system.
7. The decision taken by the International Tennis Federation to increase the size of the tennis ball by six percent is a clear disadvantage for service volley players.

Canopy reconstruction from interferometric SAR

Promotor: prof. dr. ir. R.A. Feddes
 Hoogleraar in de bodemnatuurkunde, agrohydrologie en het grondwaterbeheer

Co-promotor: dr. ir. D.H Hoekman
 Universitair hoofddocent bij het Departement Omgevingswetenschappen

Samenstelling promotiecommissie:

dr. E.A. Hendriks (Technische Universiteit Delft)
prof. ir. P. Hoogeboom (Technische Universiteit Delft)
prof. C.J. Oliver (University College/Kings College, London)
prof. dr. ir. A. Stein (Wageningen Universiteit/ITC)

2N08201, 2924

Chris Varekamp

Canopy reconstruction from interferometric SAR

Proefschrift
ter verkrijging van de graad van doctor
op gezag van de rector magnificus
van Wageningen Universiteit
prof. dr. ir. L. Speelman
in het openbaar te verdedigen
op vrijdag 12 januari 2001
des namiddags te vier uur in de Aula

1602469

To my parents

Paranimfen: Pavlik Lettinga, Martin Vissers
ISBN 90-5808-353-5

Abstract

Varekamp, C., 2000. *Canopy reconstruction from interferometric SAR*. Doctoral thesis, Wageningen University, The Netherlands.

Interferometric Synthetic Aperture Radar (InSAR) is investigated as a method for 3D tree mapping. When operational, the method may be important for monitoring forests with a persistent cloud cover such as tropical rain forests. The problem of crown displacement due to lay-over in a vegetation with a large vertical variation in scatterer height is studied. It is shown that crown displacements can be corrected for, by using coherence. An analytical expression for the coherence is derived which can be used for crown position corrections. The model is validated and shown to be consistent with observations. The water cloud model has been extended with interferometric phase, coherence and crown geometry. This model is used to simulate realistic InSAR images of a 3D forest canopy using measurements of 1064 trees. It is validated by comparing observed with simulated image statistics. The normalised second intensity moment, coherence histogram and coherence autocorrelation in range direction are used for this purpose. Results indicate a good agreement at C-band for an extinction coefficient of 0.3 m^{-1} . Two image transforms are derived based on Gaussian scattering assumptions. These transforms may be used for automated canopy reconstruction. Finally, the simulation method and the intensity image transform are used to study the effect of InSAR system parameters on the position accuracy.

Key-words: Interferometry, synthetic aperture radar, lay-over, Van Cittert-Zernike Theorem, inversion, spatial filtering, template matching, tropical forest.

Contents

Abstract	5
List of symbols	11
1 General introduction	15
1.1 InSAR for tree mapping	15
1.2 Experiment description	17
1.3 Thesis objective and overview	18
2 Position reconstruction using coherence	19
2.1 Introduction	19
2.2 Theory	21
2.2.1 Model for the coherence	21
2.2.2 Models for the volume backscattering coefficient $\sigma_v(z')$. . .	23
2.2.3 Bias of emergent tree crown position reconstruction	26
2.2.4 Calibration of the correction equations	27
2.3 Experimental	29
2.3.1 Interferometric SAR data	29
2.3.2 Field measurements of individual trees	30
2.3.3 Crown identification and data extraction	31
2.4 Results and discussion	33
2.4.1 Coherence modelling	33
2.4.2 Interferometric height and simple position reconstruction . .	34
2.4.3 Calibrated tree crown position reconstruction	36
2.5 Conclusions	37

3	InSAR Image Simulation	39
3.1	Introduction	39
3.2	Theory	40
3.3	Simulation procedure	42
3.4	Method for comparing observed with simulated data	44
3.5	Experimental	45
3.5.1	InSAR data	45
3.5.2	Field measurements	46
3.6	Results and discussion	47
3.7	Conclusions	51
4	Canopy reconstruction theory	53
4.1	Introduction	53
4.2	Data probability density functions	54
4.3	Simulated templates	55
4.4	Likelihood ratio image transform	56
4.5	Solution to the multiple response problem	58
4.6	Phase unwrapping and position calculation	59
4.7	Combining orthogonal tracks	59
4.8	Conclusions	60
5	Effect of system parameters	61
5.1	Introduction	61
5.2	Theory	61
5.2.1	Effect of baseline length	61
5.2.2	Effect of incidence angle	62
5.2.3	Effect of thermal noise power	62
5.2.4	Effect of number of looks (or resolution)	63
5.3	Experimental	63
5.4	Results and discussion	64
5.5	Conclusions	64
6	Questions and recommendations	69
6.1	Is the scattering model appropriate?	69
6.2	What are new developments?	69
6.3	How to proceed?	70

Contents	9
A Derivation of equation (2.2)	71
B Position of the scattering phase centre	73
Summary	75
Samenvatting	77
Bibliography	82
Acknowledgements	83
List of publications	85
Curriculum Vitae	87

List of symbols

SYMBOL	UNIT	DESCRIPTION
a	V m^{-1}	Complex backscattering amplitude
a	—	Fraction of backscatter contributed by upper scattering layer
b	—	Fraction of backscatter contributed by lower scattering layer
B	m	Baseline length
B_x	m	Baseline component in x -direction
B_y	m	Baseline component in y -direction
B_z	m	Baseline component in z -direction
B_n	m	Baseline component normal to line of sight
B_p	m	Baseline component parallel to line of sight
C	$\text{V}^2 \text{ m}^{-2}$	Mean of the cross-product $E_1 E_2^*$
d	m	Thickness of scattering layer
d_l	m	Thickness of lower scattering layer
d_u	m	Thickness of upper scattering layer
d_h	m	Scattering layer separation
E	V m^{-1}	Complex electric field amplitude
E_1	V m^{-1}	Complex electric field amplitude antenna 1
E_2	V m^{-1}	Complex electric field amplitude antenna 2
f	GHz	Centre frequency
H	m	Operating altitude
$H_{\hat{\sigma}}$	—	Likelihood ratio transform of $\hat{\sigma}$
$H_{\hat{\sigma}_1, \hat{\sigma}_2, \hat{C}}$	—	Likelihood ratio transform of $\hat{\sigma}_1, \hat{\sigma}_2$ and \hat{C}
i	—	Image azimuth pixel number
i_0	—	Image azimuth pixel number of shape centre point

SYMBOL	UNIT	DESCRIPTION
I_1	W m^{-2}	Mean intensity antenna 1
I_2	W m^{-2}	Mean intensity antenna 2
$I^{(2)}$	—	Normalised second intensity moment
j	—	Image range pixel number
j_0	—	Image range pixel number of shape centre point
k	—	Index variable
K_n	$\text{V}^2 \text{m}^{-4}$	Noise gain function
K_s	$\text{V}^2 \text{m}^{-4}$	Signal gain function
K_v	$\text{V}^2 \text{m}^{-1}$	Volumetric gain function
L	—	Number of looks
m	—	Transmit/receive mode of operation
n	V m^{-1}	SAR system noise
n_1	V m^{-1}	SAR system noise antenna 1
n_2	V m^{-1}	SAR system noise antenna 2
N	—	Number of pixels
N_d	—	Number of detections
N_v	m^{-3}	Number of particles per unit volume
O	—	Origin of coordinate system
r	m	Range coordinate
r_0	m	Range coordinate shape centre point
r_1	m	Range coordinate antenna 1
r_2	m	Range coordinate antenna 2
R	—	image region
s	unit[s]	crown shape vector
S	—	Binary forest structure function
V	m^3	Range cell volume
W	—	Radar impulse response function
W_1	—	Radar impulse response function antenna 1
W_2	—	Radar impulse response function antenna 2
x	m	Azimuth coordinate
x_1	m	Azimuth coordinate antenna 1

SYMBOL	UNIT	DESCRIPTION
x_2	m	Azimuth coordinate antenna 2
y	m	Ground range coordinate
y_c	m	Corrected ground range coordinate
z	m	Height coordinate
z_c	m	Corrected height coordinate
$z_{2\pi}$	m	Height of ambiguity
α	m^{-1}	Extinction coefficient
β	rad m^{-1}	Height sensitivity
γ	—	Backscattering coefficient per unit projected area
δ_r	m	Range resolution
δ_x	m	Azimuth resolution
δ_i	m	Azimuth pixel spacing
δ_j	m	Range pixel spacing
$\delta(\cdot)$	—	Dirac delta function
$\Delta\omega$	$\text{unit}[\omega]$	Increment in ω
ζ	m	Local coordinate orthogonal to propagation and azimuth direction
η	m	Local coordinate parallel to propagation direction
θ	°	Incidence angle
λ	m	Wavelength
ξ	m	Local coordinate parallel to azimuth direction
Π	—	Product
ρ	—	Coherence
ρ^{temp}	—	Coherence template
$ \rho _{\text{noise}}$	—	Noise coherence magnitude
$ \rho _{\text{volume}}$	—	Volume coherence magnitude
$ \rho _{\text{slanrange}}$	—	Slant range coherence magnitude
σ	m^2	Radar cross-section
σ^{temp}	m^2	Radar cross-section template
σ_g	m^2	Radar cross-section of ground surface
σ_b	m^2	Particle backscattering cross-section
σ_e	m^2	Particle extinction cross-section

SYMBOL	UNIT	DESCRIPTION
σ_v	$\text{m}^2 \text{m}^{-3}$	Volume backscattering coefficient
$\sigma_{v,l}$	$\text{m}^2 \text{m}^{-3}$	Volume backscattering coefficient of lower scattering layer
$\sigma_{v,u}$	$\text{m}^2 \text{m}^{-3}$	Volume backscattering coefficient of upper scattering layer
σ^0	$\text{m}^2 \text{m}^{-2}$	Backscattering coefficient
σ_l^0	$\text{m}^2 \text{m}^{-2}$	Backscattering coefficient of lower scattering layer
σ_u^0	$\text{m}^2 \text{m}^{-2}$	Backscattering coefficient of upper scattering layer
Σ	—	Sum
ϕ_1	rad	Phase of E_1
ϕ_2	rad	Phase of E_2
ϕ_s	rad	Random phase of scattering
ϕ_u	rad	Unwrapped phase difference
$\phi_{0,u}$	rad	Unwrapped phase difference of shape centre point
$\phi_{0,w}$	rad	Wrapped phase difference of shape centre point
\otimes	—	Convolution
$*$	—	Complex conjugation
$\langle \omega \rangle$	unit[ω]	Ensemble average, mean value of ω
me[ω]	unit[ω]	mean error of ω
mae[ω]	unit[ω]	mean absolute error of ω
mse[ω]	unit[ω^2]	mean square error of ω
std[ω]	unit[ω]	standard deviation of ω
var[ω]	unit[ω^2]	variance of ω

Chapter 1

General introduction

1.1 InSAR for tree mapping

Synthetic Aperture Radar (SAR) is a coherent active microwave imaging method that achieves high azimuth resolution by utilizing the Doppler spread of the echo signal [4], [8]. As an active system, SAR provides its own illumination independent of sunlight. Unlike optical systems, SAR can operate under most weather conditions because microwaves can penetrate clouds, fog and precipitation. Interferometric SAR (InSAR) uses the phase differences of at least two complex-valued SAR images acquired from different positions and/or at different times [4]. The method was introduced by Graham [18] in 1974 for measuring earth topography. Since then, InSAR has been used for measuring effects of earthquake activity and other geophysical phenomena [26].

This thesis investigates whether InSAR can be used for 3D mapping of tropical rain forest trees. Tree level monitoring of tropical forest is needed to enforce national legislation for sustainable forest management and to verify implementation of guidelines for sustainable forest management as proposed by the International Tropical Timber Organization (ITTO). Specifically, systems should be available to monitor logging activities and to detect illegal logging, allowing timely action to be taken. Because cloud cover severely limits the application of aerial photography [14], the use of airborne radar is proposed as an appropriate alternative.

To study the potential of radar, the Indonesian Radar Experiment (INDREX) campaign was executed in Indonesia in 1996 under the auspices of the Indonesian Ministry of Forestry (MOF) and the European Space Agency (ESA). The

Dornier SAR system [11] collected data in several modi over Dipterocarp rain forest test sites in the provinces East-Kalimantan (Borneo) and Jambi (Sumatra). In the same period aerial photographs were acquired and ground observations were made. Parameters such as tree 3D position, tree crown dimensions, canopy cover and terrain slope angle, as well as the location of skid trails and logging roads, are of particular interest. In principle such information can be retrieved on a routine basis over large areas from aerial photographs. Repetitive observation would allow assessment of logging intensity, erosion and fire susceptibility, as well as the verification of reforestation obligations. However, cloud cover too often prevents timely observation.

Radar does not have this limitation. Short wave, high-resolution radar may in principle give sufficient information. However, since other physical mechanisms underlie radar imaging, these images can not be treated in the same way as aerial photographs. Notably effects of *lay-over* and *radar shadow* should be handled with care. Lay-over, for instance, occurs where two tree crowns of different heights are located at the same range distance. In conventional non-interferometric radar images these two tree crowns will be imaged on top of each other, without the possibility to detect such a situation. In interferometric images this situation can be detected through the measurement of (phase) coherence. In tropical forests, height differences between individual trees can be substantial. Emergent trees in primary and logged-over forests can reach more than 10 m above other upper canopy trees. The same is true for secondary forest, which often comprises remnants of the former primary forest.

A major part of this thesis deals with the *inverse problem* [19], [5], termed canopy reconstruction: the detection of tree crowns in radar images, and the estimation of crown 3D position, size and shape. To reconstruct the forest from the inherently ambiguous and noisy radar data, one must rely on approximate solutions, satisfying additional a-priori constraints. Very often these types of inverse problems are solved iteratively with segmentation methods. A popular approach is the use of pixel-based Markov random fields as local prior models [15], [28], [25]. In this approach, prior spatial constraints are incorporated by treating each pixel variable as a random variable that is conditionally dependent on neighbouring pixel variables. A different approach is taken here. Crown shape parameters and the known scattering geometry are used explicitly to produce speckle free template

images. These templates are then used in an optimal filtering operation for detecting crowns, and for the estimation of crown 3D position, size and shape. In this way, all knowledge currently available about InSAR imaging of trees, deterministic as well as stochastic in nature, is used for inversion.

1.2 Experiment description

In this thesis, X- and C-band interferometric SAR data acquired by the Dornier SAR instrument during the INDREX 1996 campaign in Kalimantan are analysed. The test sites include the Wanariset research forest, the ITTO test site for forest rehabilitation and the ITCI concession [2]. Various InSAR tracks covered these sites. In this thesis, tracks Kal.15A, Kal.17A, Kal.18A and Kal.19C are used. Table 1.1 lists relevant sensor and image acquisition parameters. Two sets of

Table 1.1: Dornier SAR sensor and image parameters for tracks Kal.15A, Kal.17A, Kal.18A and Kal.19C of the INDREX 1996 campaign.

Parameter	Kal.15A	Kal.17A	Kal.18A	Kal.19C
Centre frequency, f (GHz)	9.6	5.3	5.3	5.3
Chirp bandwidth (MHz)	100	100	100	100
Polarization	VV	VV	VV	VV
Operating altitude, H (m)	3267	3238	3243	3228
Horizontal baseline component (m)	0.065	0.115	0.115	0.115
Vertical baseline component (m)	0.781	0.744	0.744	0.744
Transmit receive mode (-)	1	2	2	2
Swath width (m)	2000	2000	2000	2000
Incidence angle range ($^{\circ}$)	48-63	48-63	48-63	48-63
Number of independent looks	4	4	4	4
Range resolution (m)	1.75	1.75	1.75	1.75
Azimuth resolution (m)	0.31	0.34	0.47	0.34
Range pixel spacing (m)	1.25	1.25	1.25	1.25
Azimuth pixel spacing (m)	1.24	1.37	1.89	1.36

ground observations will be used in this study. The first set contains measurements of 42 trees and their lay-over geometry. These trees were selected specifically for the purpose of testing models relating the coherence magnitude to lay-over geometry. This set of observations will be used in Chapter 2. The second set of ground observations contains measurements, taken in an area of $300\text{ m} \times 240\text{ m}$, of all trees

(1064 in total) that have a diameter at breast height larger than 20 cm. The measurements included the relative position of tree stems, the relative position of tree crowns, and crown geometry. This second set of observations will be used in Chapter 3.

1.3 Thesis objective and overview

The operational problems described so far indicate that there is a need for a thorough understanding of high-resolution InSAR imaging of tropical forest. *The objective of this thesis is to evaluate InSAR as a new method for forest canopy reconstruction.* Crown spatial positions (x, y, z) and crown dimensions are forest characteristics that show an observable effect in the InSAR images because crown branches and leaves are the main scatterers at X- and C-band. Scattering by tree trunks and the ground will be ignored.

Chapter 2 concentrates on the lay-over problem: two tree crowns with considerable height difference may be imaged into the same resolution cell, resulting in a scattering phase centre that is located somewhere along the line connecting the two crown positions. By introducing a simple model for the coherence, it will be shown that the coherence measurement allows for a 3D position correction of the highest tree crown.

Chapter 3 introduces an InSAR image simulation method that will be used to compare different InSAR system configurations (Chapter 5). The InSAR image simulation method is validated by using a geometric forest model that is constructed from ground observations. After registration of the simulated and observed images, a validation is made by using a statistical approach.

Chapter 4 formulates a theory for optimal statistical canopy reconstruction using assumptions about the random nature of scattering from vegetation.

In Chapter 5 the InSAR image simulation method developed in Chapter 3 and the theory of Chapter 4 are used together to compare different InSAR system configurations. The effects of interferometric baseline length, incidence angle, thermal noise power and number of looks (resolution) are investigated.

Chapter 6 poses remaining questions and provides some guidelines for future research.

Chapter 2

Height and position reconstruction of trees using coherence

2.1 Introduction

In theory the problem of lay-over may be solved to a large extent by making use of the observed interferometric phase coherence. Loss of coherence is indicative of lay-over and can be modelled as a function of vegetation height differences. The larger the height differences in a certain range cell the lower the observed coherence. This effect has been termed *geometric decorrelation* [30, p. 148] and *spatial baseline decorrelation* [42]. Expressions for the complex degree of coherence as a function of vegetation height have been given in [30] and [20, p. 331]. The authors in [30] note that the geometric part of the coherence is an extension of the Van Cittert-Zernike theorem [7], [43] from two to three dimensions. The equivalence of InSAR with Δk -radar is treated in [31], thus allowing the use of ground-based scatterometers for detailed experiments. To our knowledge results from such ground experiments have not yet been published. Detailed modelling and validation for a homogeneous vegetation layer has been done in [38] using the TOPSAR instrument.

This Chapter concentrates on the *lay-over problem*. The observed coherence as found for emergent trees is compared with predictions using a simple model for the phase coherence. One may expect that both the three-dimensional shape of the tree crown and attenuation effects inside the tree crown will influence the phase

coherence. Both these effects are ignored in this Chapter. The first reason to do so is that most tropical trees have crowns with a rather irregular and open branch structure as illustrated in Fig. 2.1. Scattering will therefore originate from all

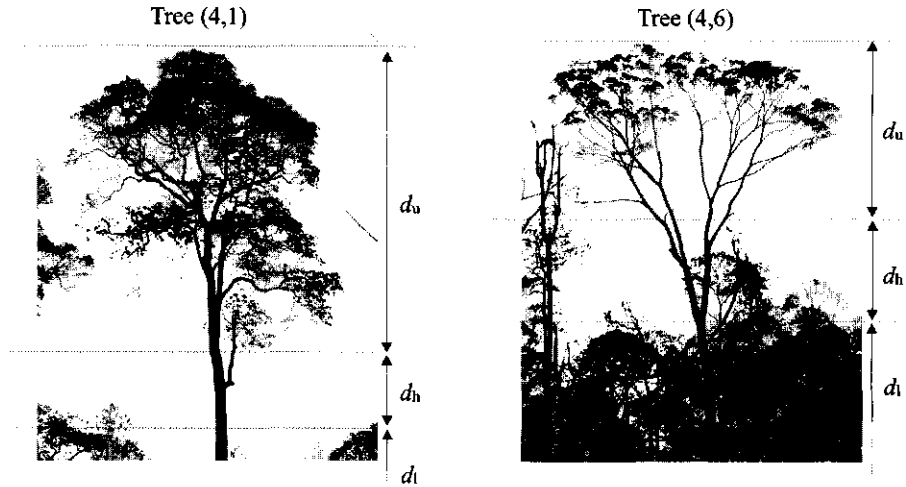


Figure 2.1: Two photographs of typical trees imaged by track Kal.19C. The layer dimensions d_l and d_u and the layer separation d_h given in the photographs are only indicative of the real measurements.

over the crown volume and attenuation is a complicated function of crown shape and scatterer parameters. Secondly, to allow for successful inversion the number of parameters in the model should be kept as small as possible.

Also the effect of the trunk-ground interaction has been ignored. This effect may be relevant in some forest types, especially for HH-polarization at small incidence angles [32]. It has been one of the considerations to conduct this experiment at large incidence angles and at VV-polarization. Moreover, most trunks are located on slopes, the crown coverage is very high and a shrub layer is usually present, which further diminishes the relevance of this term.

It will be shown that this simplified approach allows for a 3D position correction of the highest tree when two crowns with considerable height difference are mapped into the same resolution cell. Application of this simple model may be basic to the development of inversion algorithms for automated production of 3D tree maps.

2.2 Theory

2.2.1 Model for the coherence

The following derivation is similar to the one given in [20, p.331]. Radiation extinction as well as backscattering from the ground and from stems are ignored for reasons pointed out in the introduction. The mean cross-product $\langle E_1(x_1, r_1)E_2^*(x_2, r_2) \rangle$ can then be written as [22, p.87], [17]

$$\begin{aligned} \langle E_1(x_1, r_1)E_2^*(x_2, r_2) \rangle &= K_s \int_V \sigma_v(x', y', z') \exp \left(i \frac{2\pi m}{\lambda} (r'_1(y', z') - r'_2(y', z')) \right) \\ &\quad \times W(x_1 - x', r_1 - r'_1(y', z')) \\ &\quad \times W^*(x_2 - x', r_2 - r'_2(y', z')) dV' \end{aligned} \quad (2.1)$$

where E_1 and E_2 are the electric field strengths of the signals received by antennas 1 and 2, (x_1, r_1) and (x_2, r_2) are the azimuth and range coordinates of image 1 and 2, K_s is the signal gain function, λ the wavelength (m), σ_v is the volume backscattering coefficient (m^2m^{-3}), W is the radar impulse response function, V is a range cell volume (m^3) and dV' is an elementary volume $dx'dy'dz'$. The symbol m denotes the transmit/receive mode of operation: $m = 1$ for transmitting with one antenna and receiving with both antennas; $m = 2$ for transmitting and receiving with the same antenna and toggling between the upper and lower antenna [11]. The latter mode ($m = 2$) doubles the height sensitivity of the interferometer, and is often referred to as *ping pong* mode. Function K_s contains a number of contributions that must be accounted for by calibration, including the radar transmitter(s), receiver(s) and the SAR correlator. See [12, p.1112] and [8] for a detailed description. The unprimed coordinates in (2.1) correspond to a reference point for the impulse response whereas primed coordinates correspond to the location of scattering. A simplified interferometric SAR geometry is shown in Fig. 2.2. To arrive at a useful expression for the coherence magnitude $|\rho|$, the following assumptions are made:

1. The *paraxial* approximation can be used for r_1 and r_2
2. Registration of the complex SAR signals from antennas 1 and 2 causes a decorrelation that can be ignored
3. $\sigma_v(x', y', z') = \sigma_v(z')$ resulting in a one-dimensional model

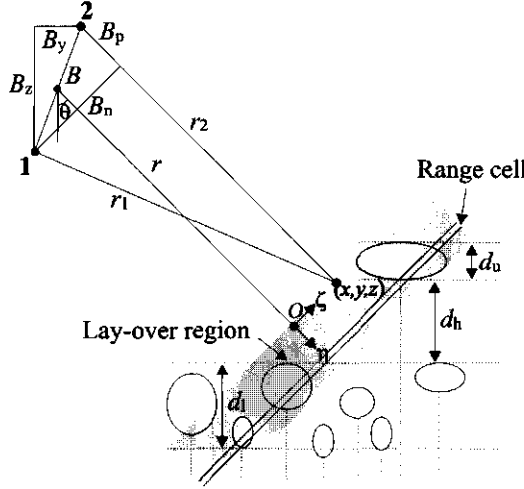


Figure 2.2: InSAR geometry and scattering configuration. The antenna positions are numbered as 1 and 2 and are separated by the baseline distance B . A local coordinate system (η, ζ) has been defined with the origin O halfway the line connecting two effective scattering layers. The thickness of the upper and lower effective scattering layers are indicated by d_u and d_l , while d_h is the distance between these layers.

4. $\langle |E_1|^2 \rangle = \langle |E_2|^2 \rangle$ due to near identical view directions

5. The noise contributions to E_1 and E_2 are uncorrelated with equal intensity.

Under these assumptions, the coherence magnitude can be expressed as the product of 'noise' coherence, volume coherence, and slant range coherence magnitudes [1].

$$\begin{aligned}
 |\rho| &= \frac{K_s \int \sigma_v(z') dz'}{K_s \int \sigma_v(z') dz' + K_n |n|^2} \\
 &\times \frac{\left| \int \sigma_v(z') \exp \left(i \frac{2\pi m B_n}{\lambda r \sin \theta} z' \right) dz' \right|}{\int \sigma_v(z') dz'} \\
 &\times \left| \iint |W(\xi', \eta')|^2 \exp \left(i \frac{2\pi m B_n}{\lambda r \tan \theta} \eta' \right) d\xi' d\eta' \right| \\
 &= |\rho|_{\text{noise}} |\rho|_{\text{volume}} |\rho|_{\text{slanrange}}.
 \end{aligned} \tag{2.2}$$

See Appendix A for the derivation of (2.2). In the next sections it is assumed that $|\rho|_{\text{noise}} = |\rho|_{\text{slanrange}} = 1$. The validity of this approximation will be shown later in Section 2.3.2.

2.2.2 Models for the volume backscattering coefficient $\sigma_v(z')$

Equation (2.2) contains one single forest dependent function: the volume backscattering coefficient as a function of height ($\sigma_v(z')$). Two criteria are important for selecting a suitable function $\sigma_v(z')$. First, $\sigma_v(z')$ must be simple to allow for accurate inversion with a small number of parameters. Second, $\sigma_v(z')$ must be an accurate representation of the vertical distribution of forest backscattering. This trade-off between model simplicity and accuracy motivates us to select not a single representation, but to try four different functions $\sigma_v(z')$ and evaluate their suitability for inversion. Consider a lay-over situation where a tall tree extends above the other trees (Fig. 2.3). Two effective scattering layers with thickness d_l and d_u

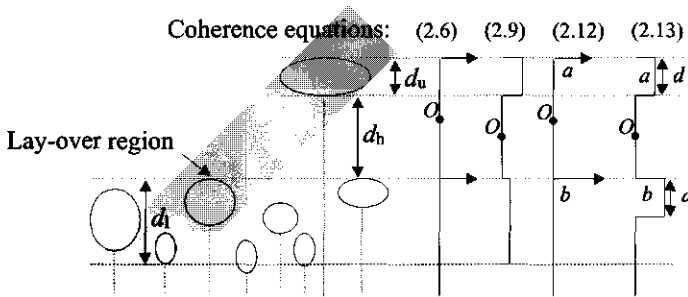


Figure 2.3: Schematic illustration of effective scattering layers together with a schematic representation of the four functions used to describe the vertical distribution of the volume backscatter coefficient $\sigma_v(z')$. The four functions for $\sigma_v(z')$ result in four equations for the coherence magnitude $|\rho|$ as expressed in (2.6), (2.9), (2.12) and (2.13). These simplified equations for $|\rho|$ were obtained using different locations for the coordinate origin O . The variables a and b are the backscattering contributions from the upper and the lower scattering layer.

separated by distance d_h are shown. The upper layer with thickness d_u represents a single emergent tree crown whereas the lower layer represents the lay-over region with thickness d_l . The volume backscattering coefficient is assumed to be only a function of z'

$$\sigma_v(z') = \sigma_{v,u}(z') + \sigma_{v,l}(z') \quad (2.3)$$

with $\sigma_{v,u}(z')$ and $\sigma_{v,l}(z')$ the volume backscattering coefficients ($\text{m}^2 \text{m}^{-3}$) for the upper and lower effective scattering layers, respectively. It seems reasonable to assume that the backscatter coefficient σ^0 ($\text{m}^2 \text{m}^{-2}$) for an emergent tree (in isolation, i.e. without its lay-over region) approximates the average backscattering

coefficient of the forest. Because emergent tree crowns are imaged as lay-over regions, the backscattering coefficient is expected to be about twice as high due to the contribution of the lower vegetation layer. This was verified by comparing the average intensity of a large image subset of 2000 azimuth by 1000 range pixels to the average intensity of a large number of lay-over regions of emergent trees. The average image intensity for the lay-over regions of emergent trees was found to be 1.80 times the average image intensity of the large image subset. Consequently, it may be assumed that on average σ_u^0 is slightly lower than σ_l^0 with

$$\sigma_u^0 = \int \sigma_{v,u}(z') dz' \text{ and } \sigma_l^0 = \int \sigma_{v,l}(z') dz'. \quad (2.4)$$

The two-layer geometry can now be used to specify four different functions for $\sigma_v(z')$ which will be discussed in detail. The first two functions represent different scattering geometries related to forest structure. The second two functions extend the first two functions by allowing the backscattering coefficient of the upper layer to differ from the backscattering coefficient of the lower layer. Radar shadow, decreasing the contribution of the lower layer, is the main motivation for this extension. The four functions for $\sigma_v(z')$ will result in four equations for the coherence magnitude $|\rho|$. In the following these coherence models will be referred to as: the symmetric delta function (2.6), the symmetric rectangular function (2.9), the asymmetric delta function (2.12) and the asymmetric rectangular function (2.13).

Symmetric delta function

The first function for $\sigma_v(z')$ simply assumes two scattering points (Fig. 2.3)

$$\sigma_v(z') = \sigma_u^0 \delta\left(z' - \frac{d_h + d_u}{2}\right) + \sigma_l^0 \delta\left(z' + \frac{d_h + d_u}{2}\right) \quad (2.5)$$

with $\delta(z')$ the Dirac delta function (m^{-1}). Both scattering points lie at the top of their respective layer which means that the points are separated by a distance $d_h + d_u$. Next, equal scattering of both points is assumed: $\sigma_u^0 = \sigma_l^0$. Using (2.5) in (2.2) gives for the coherence magnitude

$$\begin{aligned} |\rho| &= |\rho|_{\text{noise}} |\rho|_{\text{volume}} |\rho|_{\text{slant range}} \\ &= \left| \frac{e^{i\beta\left(\frac{d_h+d_u}{2}\right)} + e^{-i\beta\left(\frac{d_h+d_u}{2}\right)}}{2} \right| \\ &= \left| \cos\left(\beta\left(\frac{d_h+d_u}{2}\right)\right) \right|, \end{aligned} \quad (2.6)$$

where

$$\beta = \frac{2\pi m B_n}{\lambda r \sin \theta}. \quad (2.7)$$

Fig. 2.4 illustrates $|\rho|$ as a function of $d_h + d_u$.

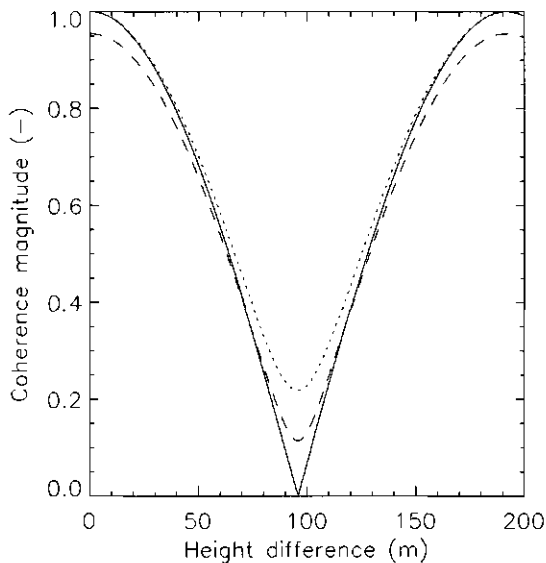


Figure 2.4: Plot of coherence magnitude $|\rho|$ versus $d_h + d_u$. Symmetric delta function (solid line); Asymmetric delta function with $a = 0.629$ (short dash); Asymmetric rectangular function with equal layer thicknesses $d_l = d_u = d$ (long dash). The parameter values of this rectangular function are: $a = 0.56$ and $d = 32$ m. The following InSAR system dependent variables were used: $\theta = 54.7^\circ$, $r = 5592$ m, $B_n = 0.674$ m, $m = 2$.

Symmetric rectangular function

The second function for $\sigma_v(z')$ assumes a rectangular function for $\sigma_{v,u}(z')$ and $\sigma_{v,l}(z')$ and equal scattering of both layers, i.e. $\sigma_u^0 = \sigma_l^0$ (Fig. 2.3):

$$\sigma_v(z') = \sigma_u^0 \chi\left(\frac{d_h}{2}, \frac{d_h}{2} + d_u\right) + \sigma_l^0 \chi\left(-\frac{d_h}{2} - d_l, -\frac{d_h}{2}\right) \quad (2.8)$$

with

$$\chi(z_1, z_2) = \begin{cases} \frac{1}{z_2 - z_1} & (z_1 < z' < z_2) \\ 0 & \text{otherwise} \end{cases}.$$

Now $|\rho|$ follows as:

$$|\rho| = \left| \frac{e^{-i\frac{2\pi m B_p}{\lambda}}}{i2\beta} \left(\frac{1}{d_u} \left(e^{i\beta\left(\frac{d_h}{2} + d_u\right)} - e^{i\beta\left(\frac{d_h}{2}\right)} \right) + \frac{1}{d_l} \left(e^{-i\beta\left(\frac{d_h}{2}\right)} - e^{-i\beta\left(\frac{d_h}{2} + d_l\right)} \right) \right) \right|. \quad (2.9)$$

Asymmetric delta function

As a more general case, it can be assumed that backscattering of the upper layer differs from the lower layer. When the fractions a and b are introduced as (Fig. 2.3):

$$a = \frac{\sigma_u^0}{\sigma_u^0 + \sigma_l^0} \quad (2.10)$$

and

$$b = \frac{\sigma_l^0}{\sigma_u^0 + \sigma_l^0} \quad (2.11)$$

then, (2.6) can be rewritten as:

$$|\rho| = \left| e^{-i\frac{2\pi m B_p}{\lambda}} \left(a e^{i\beta\left(\frac{d_h + d_u}{2}\right)} + (1 - a) e^{-i\beta\left(\frac{d_h + d_u}{2}\right)} \right) \right|. \quad (2.12)$$

Asymmetric rectangular function

Using again the fractions a and b , (2.9) can be rewritten as:

$$|\rho| = \left| \frac{e^{-i\frac{2\pi m B_p}{\lambda}}}{i\beta} \left(\frac{a}{d_u} \left(e^{i\beta\left(\frac{d_h}{2} + d_u\right)} - e^{i\beta\left(\frac{d_h}{2}\right)} \right) + \frac{(1 - a)}{d_l} \left(e^{-i\beta\left(\frac{d_h}{2}\right)} - e^{-i\beta\left(\frac{d_h}{2} + d_l\right)} \right) \right) \right|. \quad (2.13)$$

2.2.3 Bias of emergent tree crown position reconstruction

In the very simple case of the symmetric delta function for $\sigma_v(z')$, the coherence magnitude is the absolute value of a cosine function of the height difference between the top of the emergent tree and the top of the canopy in the lay-over region ((2.6) and Fig. 2.4). The solution to (2.6) is unique when

$$0 \leq \beta \left(\frac{d_h + d_u}{2} \right) \leq \frac{\pi}{2}. \quad (2.14)$$

For the system parameters mentioned in the caption of Fig. 2.4 the corresponding height difference range is $0 \leq d_h + d_u \leq 94.8$ m. Under the assumption that the

position of the scattering phase centre is halfway the true position of the tree top and the true position of its lay-over region, the observed crown coordinates y, z , for this specific range of height differences, can be corrected using (2.6) as

$$y_c = y + \frac{\lambda r \cos \theta}{2\pi m B_n} \cos^{-1}(|\rho|) \quad (2.15)$$

$$z_c = z + \frac{\lambda r \sin \theta}{2\pi m B_n} \cos^{-1}(|\rho|). \quad (2.16)$$

In case these correction equations are applied, while in reality the forest layers are asymmetric, i.e. $a \neq b$, a bias in the position reconstruction of the emergent tree results. This bias is caused by a shift of the scattering phase centre in the direction of the layer with highest backscattering and a lower reconstruction (or correction) shift towards the upper layer (since $|\rho|$ is smaller). This bias is graphically depicted in Fig. 2.5 for both the asymmetric delta function (2.12) and for the asymmetric rectangular function (2.13) with a as the asymmetry parameter. Obviously, under the assumption that the forest scattering layers can be modelled by the symmetric delta function (2.6), the correction equations (2.15) and (2.16) perform well in case there is no lay-over ($a = 1$) and in cases where there is lay-over and the backscatter of the upper and lower layers are equal ($a = 0.5$). In the latter case a large error is made when no correction is applied. For all other cases a bias results, which, for large values of a , in absolute sense even exceeds the error resulting from not applying a correction. Under the assumption that the forest layers can be modelled by a symmetric rectangular function, representing layers of 5 m thickness (in this example), and corrections (2.15) and (2.16) are applied, different biases result (see also Fig. 2.5). In general, it can be stated that the bias depends on the shapes of both upper and lower layer and that good height corrections for individual trees are only possible when these shapes are known *a priori* for each tree. In practical situations it may be feasible to adopt an *efficient average* shape, resulting in *optimised* correction equations.

2.2.4 Calibration of the correction equations

Suppose that *on average* tree positions are best corrected by assuming the asymmetric delta function. In the same way as correction equations (2.15) and (2.16) follow from (2.6), alternative correction equations now follow from (2.12) by re-

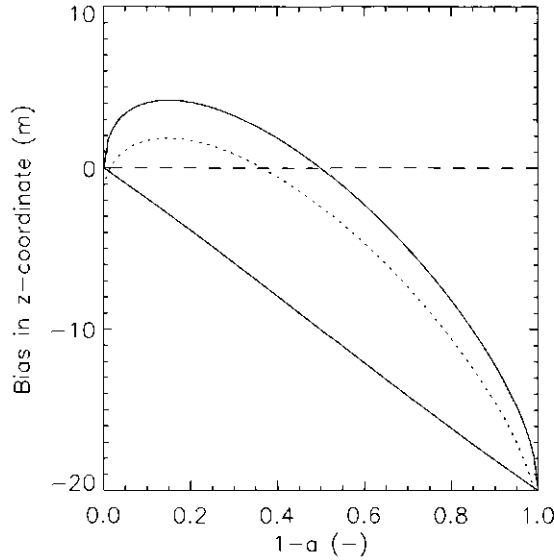


Figure 2.5: Bias of z -coordinate versus the fraction of backscatter originating from lower layer ($b = 1 - a$) for three different cases: The layers are described by an asymmetric delta function with a spacing $d_h = 20$ m and no correction is applied (lower solid line). Idem dito except that a correction is applied assuming a symmetric delta function (upper solid line). The layers are described by an asymmetric rectangular function with a spacing $d_h = 15$ m and layer thicknesses $d_l = d_u = 5$ m and a correction is applied assuming a symmetric delta function (dotted line).

placing the term $\cos^{-1}(|\rho|)$ in (2.15) and (2.16) with:

$$\sin^{-1} \left(\sqrt{\frac{1 - |\rho|^2}{(4a - 4a^2)}} \right) - \tan^{-1} \left((2a - 1) \tan \left(\sin^{-1} \sqrt{\frac{1 - |\rho|^2}{(4a - 4a^2)}} \right) \right). \quad (2.17)$$

In case a set of data with real tree heights and corrected interferometric tree heights would be available, the value of the asymmetry parameter a could be tuned to remove the bias, or to minimize the mean square error (mse), on average. Of course even more complicated correction equations may be developed, e.g. by assuming an asymmetric rectangular function with a-priori fixed thickness d representing the average layer thickness ($d_l = d_u = d$). In this case the two parameter values a and d are estimated empirically. Now alternative correction equations follow from

(2.13) by replacing the term $\cos^{-1}(|\rho|)$ in (2.15) and (2.16) with:

$$\psi = \tan^{-1} \left(\frac{(1-2a)(\cos(\psi + \beta d) - \cos \psi)}{\sin(\psi + \beta d) - \sin \psi} \right) + \beta d. \quad (2.18)$$

where

$$\psi = \sin^{-1} \left(\sqrt{\frac{\beta^2 d^2 |\rho|^2 - 2(1 - \cos(\beta d))}{2(4a^2 - 4a)(1 - \cos(\beta d))}} \right) - \frac{\beta d}{2}$$

The merit of such a semi-empirical approach is that bias removal could be better optimised, while the values of the parameters may be related to forest structure types.

2.3 Experimental

2.3.1 Interferometric SAR data

InSAR data from tracks Kal.17A, Kal.18A and Kal.19C were used for this experiment. Refer to Table 1.1 for a description of the relevant Dornier SAR sensor parameters and image acquisition parameters. The basic data types provided by Dornier were the multi-look average intensities and the complex interferogram given by:

$$\hat{I}_1 \propto \frac{1}{L} \sum_{k=1}^L |E_{1,k}|^2, \quad (2.19)$$

$$\hat{I}_2 \propto \frac{1}{L} \sum_{k=1}^L |E_{2,k}|^2 \quad (2.20)$$

and

$$\hat{\rho} = \frac{\sum_{k=1}^L E_{1,k} E_{2,k}^*}{\sqrt{\sum_{k=1}^L |E_{1,k}|^2 \sum_{k=1}^L |E_{2,k}|^2}} \quad (2.21)$$

with L the number of looks per pixel. The z -coordinate image was calculated from the phase difference $\arg(\hat{\rho})$ after phase unwrapping and using the parameters of Table 1.1. Fig. 2.6 shows slant range images of the observed intensity, the interferometric z -coordinate, and the coherence magnitude for a subset of track Kal.19C. Labeled polygons roughly indicate the positions of the crowns of large trees that were selected during fieldwork.

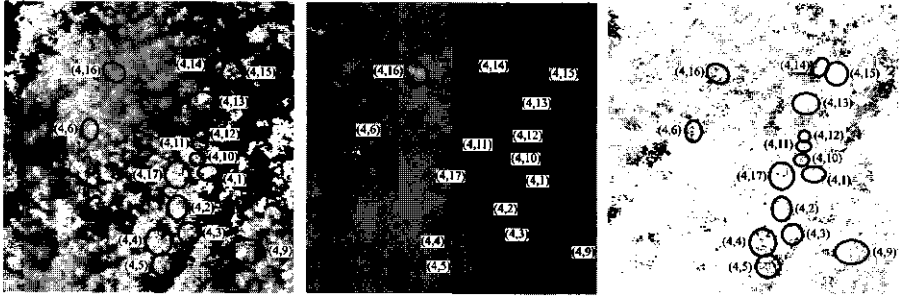


Figure 2.6: Subset of 200×200 pixels of slant range radar data of track Kal.19C covering the ITTO test site for forest rehabilitation. Images of observed intensity (left), z-coordinate (middle) and coherence magnitude (right) are shown. The z-coordinate is scaled between 75 m and 200 m. The observed intensity has a range of 41.8 dB. The coherence magnitude is scaled between 0.8 and 1. The radar look direction is from left to right.

2.3.2 Field measurements of individual trees

In situ measurements of large individual trees were made in several study sites in East-Kalimantan. Tree positions were measured relative to other trees or relative to known points on a road. For each tree, the total tree height, tree crown dimensions, the height of the tree base relative to all trees in the same study plot, and the characteristics of the terrain and vegetation in the lay-over region were measured. In addition it was noted whether the vegetation in the lay-over region was in the radar shadow of trees closer to the radar or not (Fig. 2.7). Also each tree crown was photographed from different directions. For these trees d_i , d_u and d_h were determined from the field measurements. A total of 42 trees were selected, *for which the lay-over region was not shadowed by trees closer to the radar*. The values are listed in Table 2.1. It can be seen from Table 1.1 and Table 2.1 that the resolution is fine compared to the layer dimensions d_u and d_l and the layer separation d_h . The slant range coherence magnitude $|\rho|_{\text{slanrange}}$ will decrease as a function of scattering layer thickness. Even for a scattering layer with a thickness of 50 m, $|\rho|_{\text{slanrange}} = 0.996$, which is still very close to 1. Therefore slant range decorrelation will be ignored. Decorrelation due to noise is also a small effect. Using the intensity of a smooth water surface in the far range and the intensity of forest vegetation, a SNR of 25.92 dB was found. The corresponding $|\rho|_{\text{noise}}$ follows from (2.2) and equals 0.997. Therefore noise decorrelation will be ignored. Note

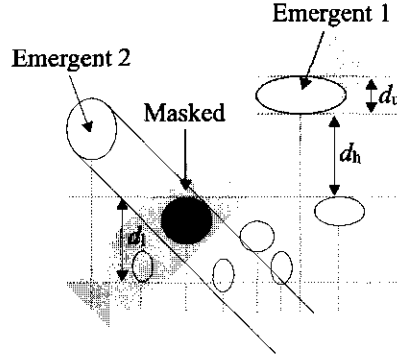


Figure 2.7: Shadowing of the lay-over region. Indicated are the thickness of the lower scattering layer d_l , the thickness of the upper scattering layer d_u and the distance between these layers d_h .

that the decorrelation due to these two effects $(1 - |\rho|_{\text{noise}} |\rho|_{\text{slant range}})$ is 0.007 which is still minor compared to the smallest total decorrelation found for the trees measured (see Table 2.1).

2.3.3 Crown identification and data extraction

The 42 tree crowns were identified in the radar images with the help of tree field drawings and tree crown photographs. The crown pixels were selected manually on the computer screen. This selection step was done using a median filtered image of the z -coordinate. A 3×3 window was used for filtering. The crown coherence magnitude was estimated by the average of all pixels in the crown region

$$|\rho| = \frac{1}{N} \left| \sum_{k=1}^N \hat{\rho}_k \right| \quad (2.22)$$

where N is the number of pixels in the crown region. The average height of pixels neighbouring crown pixels was assumed to be representative of the height of the lower layer in the lay-over region. Fig. 2.9 illustrates the two regions. For each region of neighbouring pixels the average z -coordinate was also estimated. The coherence magnitude estimates are biased and the accuracy of these estimates depends on the sample size. Table 2.2 gives an indication of the bias of the estimate for 4-look data and an indication of the large sample variance of the estimate for a sample of N uncorrelated pixels for several values of $|\rho|$ according to [37]. The

Table 2.1: Measurement of thickness of lower layer (d_l), thickness of upper layer (d_u), layer separation (d_h), number of crown pixels (N) and coherence magnitude ($|\rho|$) for 42 trees. For these trees the lay-over region was not shadowed by trees closer to the radar.

Track	Tree	d_l (m)	d_u (m)	d_h (m)	N (-)	$ \rho $ (-)
Kal.17A	17.1	9.1	25	16.7	100	0.794
Kal.17A	17.2	3.3	7	20.8	39	0.924
Kal.17A	17.3	6	16	21	105	0.807
Kal.17A	17.4	12	27	22	222	0.725
Kal.17A	17.8	2	20	40	77	0.574
Kal.17A	17.9	0.5	20	43.5	138	0.648
Kal.17A	17.35	15.7	22	6.2	139	0.908
Kal.17A	17.101	15	39.6	-2	267	0.697
Kal.17A	17.102	10	31	31	149	0.701
Kal.18A	18.1	25.3	25	2.7	129	0.774
Kal.18A	18.2	6.4	7	15.3	23	0.835
Kal.18A	18.3	21.2	16	10	71	0.753
Kal.18A	18.4	15	27	23	117	0.599
Kal.18A	18.7	40.2	20	0.1	116	0.753
Kal.18A	18.11	5	22	19	77	0.651
Kal.18A	18.35	17.3	22	16.6	79	0.732
Kal.18A	18.101	5	39.6	18	226	0.611
Kal.18A	18.102	10	31	31	162	0.639
Kal.19C	2.1	2	12.5	10	55	0.957
Kal.19C	3.1	10	13	15	43	0.921
Kal.19C	3.2	10	10	13	58	0.926
Kal.19C	3.3	10	14	11	183	0.912
Kal.19C	4.1	5	18	13	87	0.863
Kal.19C	4.2	5	10.5	16	131	0.872
Kal.19C	4.3	5	11	25	95	0.803
Kal.19C	4.4	5	18	29	192	0.759
Kal.19C	4.5	5	16	27.5	194	0.769
Kal.19C	4.6	5	19	29	168	0.720
Kal.19C	4.9	7	12	17.5	246	0.894
Kal.19C	4.10	5	15	21.5	37	0.851
Kal.19C	4.11	10	12	11	29	0.913
Kal.19C	4.12	10	19.5	-4	77	0.943
Kal.19C	4.13	10	19	3.5	128	0.955
Kal.19C	4.14	10	13	7	86	0.915
Kal.19C	4.15	10	12	10	140	0.925
Kal.19C	4.16	10	26.5	9	105	0.808
Kal.19C	4.17	5	18.75	16	101	0.861
Kal.19C	6.1	5	17.75	-4	176	0.929
Kal.19C	6.2	5	22	21	127	0.852
Kal.19C	6.3	5	19	14	134	0.850
Kal.19C	6.4	5	28	1	170	0.922
Kal.19C	6.5	5	14	17	107	0.918

number of looks specified by Dornier is 5. To verify this, and to determine the effective number of independent looks, the coherence of a river water surface in

Table 2.2: Bias $\langle |\rho| \rangle - |\rho|$ and variance $\text{var}[|\rho|]$ of the coherence magnitude estimate for several values of the mean crown coherence $|\rho|$ for 4-look data and N pixels according to [37]. Note that the variance values only apply for sufficiently large N .

$ \rho $	$\langle \rho \rangle - \rho $	$\text{var}[\rho]$
0.5	-0.024	$0.1802/N$
0.75	-0.023	$0.0971/N$
0.95	-0.007	$0.0181/N$
0.99	-0.002	$0.0034/N$

the far range was measured. Its value of 0.4659 is very close to the value of 0.4571 for 4-look data, that can be computed for a completely uncorrelated surface, and much higher than the value of 0.4063 for 5-look data [37]. Therefore, since the water surface still may show some coherence, the number of 4 can be regarded as a minimum value for the number of independent looks. By studying the image intensity of a large homogeneous rice field it could be shown that the pixels have considerable spatial correlation in range, and to a lesser extent in azimuth. As a result the number of independent pixels reduces in the worst case to 38% of the sample sizes indicated in Table 2.1. In this worst case, i.e. for $|\rho| = 0.5$ and for the minimum number of pixels, i.e. $N = 23$, the standard deviation of the estimate can be calculated as 0.141. In practice the standard deviations are much lower, because $|\rho|$ is usually much higher and the lower values of $|\rho|$ are associated with large samples (large trees) as can be derived from Table 2.1. The bias is small for all trees and has been ignored in the analysis.

2.4 Results and discussion

2.4.1 Coherence modelling

For the 42 selected trees the observed coherence magnitude was compared with the coherence magnitude predicted according (2.6) and (2.9), i.e. the symmetric delta and symmetric rectangular functions, respectively, by substituting values for d_1 , d_u and d_h as recorded in the field. The results are shown in Fig. 2.8. Both models predict the coherence magnitude well. For the symmetric delta function the correlation between observed and predicted coherence is 0.912 and the mean error is 0.007. For the symmetric rectangular function these values are 0.942 and 0.042,

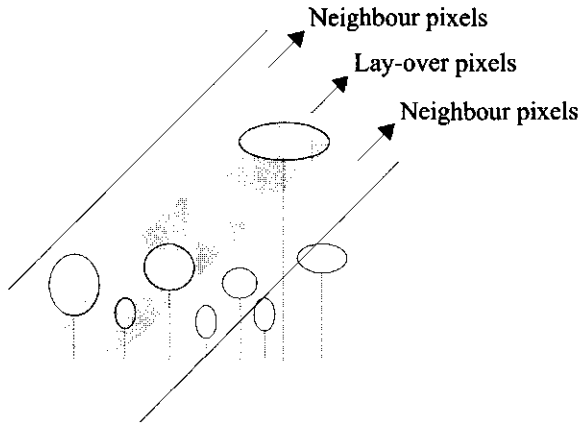


Figure 2.9: Illustration of pixels covering the lay-over region and neighbouring pixels covering the adjacent lower vegetation.

the true height difference $d_h + d_u$ as measured in the field. It clearly shows that

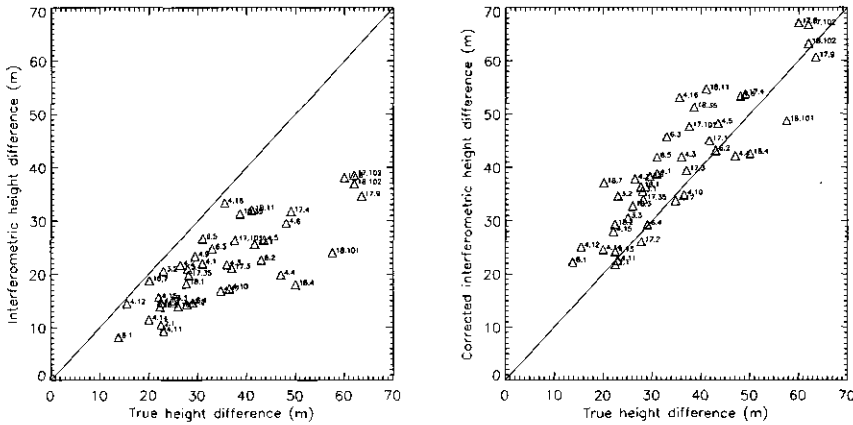


Figure 2.10: Underestimation of the true height difference (left) and interferometric height difference correction when using equation (2.16) (right)

the interferometric height difference substantially underestimates the true height differences as was expected. It is noted again that the height of the lay-over regions for these 42 emergent trees cannot be extracted from the images. However, it can be estimated by the height of the forest surrounding the lay-over region as illustrated in Fig. 2.9. Now the correction equations can be evaluated by using

these data. In Fig. 2.10 the interferometric height difference has been corrected using (2.16) (i.e. the symmetric delta function).

2.4.3 Calibrated tree crown position reconstruction

To be able to apply the asymmetric functions (i.e. using equations (2.12) and (2.13)), calibration parameters a in (2.17) and a and d in (2.18) have to be determined first. This was done by regression analysis, using all 42 selected trees. Results are shown in Fig. 2.11 and in Table 2.3. The results clearly show that

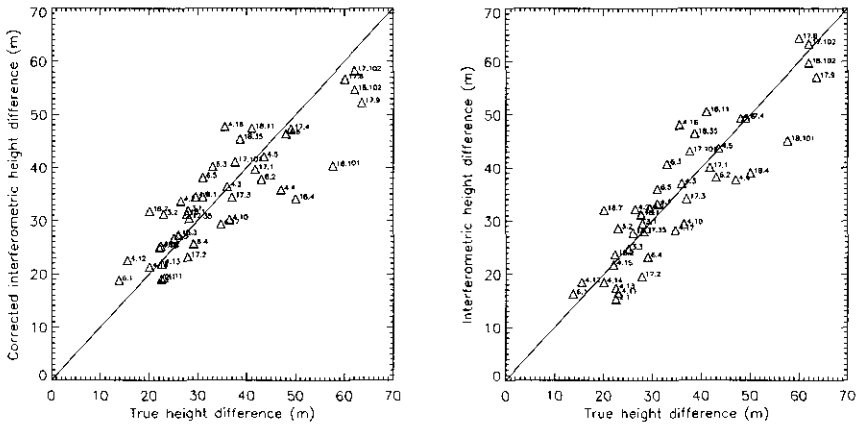


Figure 2.11: Interferometric height difference correction with (2.17) (left) and with (2.18) (right).

application of correction equations is useful and that both calibrated correction models outperform the simple correction model. Moreover, since these two models have a physical basis, the values of the fitted parameters a and d can be related to the average forest structure. In comparison to the simple correction model the asymmetric delta function reduces $\text{mse}[d_h + d_u]$ from 62.2 to 43.4. The fitted asymmetry parameter a has a value of 0.63, indicating that most of the backscatter originates from the upper layer. Such an asymmetry is in correspondence with the inference made at the end of Section 2.4.1. The calibration result of the most elaborated model, using the asymmetric rectangular function, is particularly interesting since it fits both layer thickness ($d = 32$) and backscatter asymmetry ($a = 0.56$), in such a way that reconstruction of (these 42) emergent tree positions

Table 2.3: Bias removal: Approaches, mean error $\text{me}[d_h + d_u]$ and mean square error $\text{mse}[d_h + d_u]$. Minimising $\text{mse}[d_h + d_u]$ fits the empirical parameters of the calibration models.

Approach	$\text{me}[d_h + d_u]$ (m)	$\text{mse}[d_h + d_u]$ (m ²)
No correction	-13.17	240.14
Simple correction: (2.15) and (2.16)	5.14	62.16
Calibrated correction: (2.17), $a = 0.63$	0.01	43.40
Calibrated correction: (2.18), $a = 0.56$, $d = 32$	0.48	37.94

is optimised on average. As expected when introducing an additional fit parameter, it further reduces $\text{mse}[d_h + d_u]$. However, the additional reduction from 43.4 to 37.9 is not very large. Moreover, it was observed that the minimum for the parameter d , in contrast to the minimum of the parameter a , is not well defined for this data set. In the limit of $d \rightarrow 0$ the same values are found as for the asymmetric delta function, as expected. When d is increased, the values for a and $\text{mse}[d_h + d_u]$ both decrease gently. For $d = 1$, the optimum value of a is 0.61 and $\text{mse}[d_h + d_u]$ is 42.4; for $d = 10$, $a = 0.60$ and $\text{mse}[d_h + d_u] = 41.7$; for $d = 20$, $a = 0.59$ and $\text{mse}[d_h + d_u] = 40.1$; for $d = 32$, $a = 0.56$ and $\text{mse}[d_h + d_u] = 37.9$ (the minimum); and for $d = 33$, $a = 0.56$ and $\text{mse}[d_h + d_u] = 38.1$. It is noted that for values of d in excess of 33, equation (2.18) gives no valid solution anymore for the tree with the highest coherence magnitude. It may be concluded that the forest layering can not be described well with effective mean layer dimensions. This can also be inferred from Table 2.1, showing that the thickness of the upper and lower layer vary widely. Hence, to describe the complicated structure of tropical rain forest in this way, by effective mean layer dimensions, may be an oversimplification, not resulting in major additional corrections of tree crown positions.

2.5 Conclusions

The results show that on the basis of field observations and the use of simple models for the vertical distribution of backscattering, *coherence magnitudes of emergent trees can be predicted well*. It is also shown that in interferometric images large height and displacement errors can occur for individual emergent trees and that these errors can be corrected using these simple models.

It is shown that a representation in which all backscatter is assumed to be originating from horizontal planes located at the top of the emergent tree and at the top of its lay-over region already gives a fairly good result. Further extension to horizontal layers improves the coherence magnitude modelling for individual trees. However, it seems difficult to find an 'effective' mean layer thickness, which can be used to improve correction for height and displacement errors. Apparently the structure of the tropical rain forest at the studied site is too complex to make this meaningful.

The application of correction models is useful since they give a major reduction of $\text{mse}[d_h + d_u]$. However, the value of $\text{mse}[d_h + d_u]$ itself should be interpreted with care. The correction applied is a correction based on the observed coherence magnitude of the emergent crown and its lay-over region. The (relative) interferometric height of the tree can only be measured relative to the (relative) interferometric height of its surroundings. Since the height of the surroundings of the lay-over region may differ from the height of the lay-over region an additional independent error will be introduced. In other words: the expected accuracy of height correction may be higher than the value of $\text{mse}[d_h + d_u]$ indicates. On the other hand it should be noted that the best corrections methods are based on calibrations for which the same trees are used. Moreover, such a calibration is forest structure dependent and may not give optimal results when applied to other forest types.

From a physical point of view, it is interesting to study the values of the parameters fitted for the calibration models since they reveal properties of the forest structure. For the set of 42 trees studied, for example, it could be concluded that slightly more backscatter originates from the emergent crown as compared to its lay-over region and that the concept of effective mean layers is hardly meaningful.

The results indicated in this Chapter may be very useful for the development of algorithms for automated tree map production [39]. Further physical modelling and tree mapping developments are planned using data of a fully inventoried 7.2 ha plot, for which additional X-band data and additional C-band data with a different look direction exist. The large time elapsed between INDREX radar data collection and the various field observation periods (up to 3 years now) poses some interpretation problems. For this reason a new campaign in Kalimantan is under consideration.

Chapter 3

InSAR Image Simulation

3.1 Introduction

This Chapter describes an Interferometric SAR image simulation procedure for 3D forest canopies. The procedure will be used as a tool to test tree map inversion algorithms and to compare different InSAR system configurations for tree map inversion. Before the procedure can be applied for these purposes it needs to be validated using ground truth and experimental InSAR data. *The objective of this Chapter is to validate physical assumptions made at the modelling stage.* The second set of ground observations was used for this purpose. The data set contains measurements, taken in an area of 300 m×240 m, of all trees (1064 in total) that have a diameter at breast height larger than 20 cm. These 1064 trees are used to construct a 3D forest geometry model describing the tree crowns which are the main contributing scatterers at X- and C-band. The 3D forest geometry model is then used to simulate realistic InSAR images. The simulated images are compared with observed X-band (track Kal.15A), and C-band (track Kal.17A) images acquired during the INDREX-96 airborne campaign. The InSAR simulation model is an extension of the water cloud model [3] adding interferometric phase and coherence and describing the geometry of each tree crown. Predictions are made for three values of the extinction coefficient α : 0.075 m^{-1} , 0.15 m^{-1} and 0.3 m^{-1} . The comparison is based on the normalised second intensity moment, the mean coherence magnitude, the histogram of the coherence magnitude and the autocorrelation of the coherence magnitude.

Only a few papers have been published on the simulation of SAR images of

a 3D explicit forest scene. Early work by Oliver [27] presents statistical intensity texture simulation methods based on the autocorrelation function. In the work by Sun and Ranson [34] a physical model is introduced for predicting high-resolution C-, L- and P-band intensity images of 3D forest scenes. The model requires many input parameters describing leaf and branch structure and dielectric properties. Recently, Sarabandi and Lin [33] have reported a simulation procedure for the InSAR response of coniferous trees taking into account 3D structure. They account for multiple scattering (for instance trunk-ground interactions) and therefore need as input the scattering matrix for each individual scatterer. The advantage of their approach is that absolute phase relations are described thereby accounting for interactions between a scatterer and the ground.

The simulation procedure presented in this Chapter does not include multiple scattering because it can be ignored for our purpose. *The InSAR signal is simply described by an algebraic sum of complex scattering amplitudes at different locations weighted by the mean attenuated field.* Forest variables such as crown spatial positioning, crown size, mean reflectivity, extinction and the effect of random scatterer locations are thus accounted for. Also the basic SAR system parameters resolution and receiver noise will be accounted for.

3.2 Theory

At X- and C-band, the tree crown is assumed to be an isotropic random scattering volume consisting of many independent scatterers per resolution cell (single scattering). To describe the phase and coherence of the InSAR, the *water cloud model* [3] is extended to include the random phase fluctuations due to the randomly positioned scatterers. (It is convenient to take the well known water cloud model as a starting point. The basic theory however is described with more detail in [22]). The two (complex) electric fields after detection can be described by

$$E_1(x, r) = \sqrt{K_s} \left(\int a(x, y, z) e^{i\phi_1(y, z)} r d\theta \right) \otimes W(x, r) + \sqrt{K_n} n_1 \quad (3.1)$$

$$E_2(x, r) = \sqrt{K_s} \left(\int a(x, y, z) e^{i\phi_2(y, z)} r d\theta \right) \otimes W(x, r) + \sqrt{K_n} n_2 \quad (3.2)$$

where $a(x, y, z)$ is the backscattering amplitude and $\phi_1(y, z)$, $\phi_2(y, z)$ are the two phases at antenna 1 and 2. It is assumed that cylindrical coordinates can be

used in 3.1 and 3.2, which corresponds to the zero-Doppler InSAR approximation. (Non-zero squint angle can not be simulated). K_n is the system gain in the presence of noise. It includes contributions from all the dominant noise sources including Earth's microwave background radiation, thermal noise and other sources (see [12, p.1113] for a complete description). The additive noise terms n_1 and n_2 are assumed to have equal mean intensity: $\langle |n_1|^2 \rangle = \langle |n_2|^2 \rangle \equiv \langle |n|^2 \rangle$. The convolution operation denoted by \otimes is assumed identical for both antennas, i.e.: $W_1(x, r) = W_2(x, r) \equiv W(x, r)$. Microwave backscattering and extinction are incorporated in the backscattering amplitude which obeys the following equation:

$$\langle a(x, y, z)a(x, y, z)^* \rangle = K_v N_v \sigma_b S(x, y, z) e^{-2 \int_0^r N_v \sigma_e S(x, y, z) dr} \quad (3.3)$$

where K_v is a radar equation constant, N_v is the number of particles per unit volume (m^{-3}), σ_b is the particle backscattering cross-section (m^2), and σ_e is the particle extinction cross-section (m^2).

This thesis work extends the water cloud model from one spatial dimension to three spatial dimensions by inclusion of a 3D binary forest structure function which models tree crown spatial position and crown geometry:

$$S(x, y, z) = \begin{cases} 1 & \text{inside a crown volume} \\ 0 & \text{outside a crown volume.} \end{cases} \quad (3.4)$$

A further extension of the water cloud model is the explicit description of the stochastic nature of scattering. Random fluctuations are introduced into the model by assuming that scatterers have *independent uniform random* (x, y, z) -coordinates. If the resolution cell is many wavelengths across, the phase of the radar measurement will also vary uniform randomly on domain $(-\pi, \pi)$. The phases of E_1 and E_2 can therefore be written as the sum of a deterministic term different for both antennas, and dependent of InSAR geometry, plus a uniform random phase of scattering ϕ_s identical for both antennas:

$$\phi_1(y, z) = \frac{2\pi m}{\lambda} \sqrt{r^2 + \frac{B^2}{4} + rB \cos \left(\theta + \tan^{-1} \left(\frac{B_y}{B_z} \right) \right)} + \phi_s \quad (3.5)$$

$$\phi_2(y, z) = \frac{2\pi m}{\lambda} \sqrt{r^2 + \frac{B^2}{4} - rB \cos \left(\theta + \tan^{-1} \left(\frac{B_y}{B_z} \right) \right)} + \phi_s \quad (3.6)$$

where

$$r = \sqrt{(H - z)^2 + y^2}, \quad (3.7)$$

$$\theta = \tan^{-1} \left(\frac{y}{H - z} \right), \quad (3.8)$$

B is the baseline length and B_y , B_z are the baseline components in y - and z -direction. The baseline component in x -direction (B_x) is assumed zero. When the number of scatterers per resolution cell is large, the resulting random variables E_1 and E_2 each have a *complex circular Gaussian* probability density function. This result follows directly from the central limit theorem. Refer to [9, p.15] for proof. Finally, an idealised radar impulse response function (also termed resolution function) is assumed [30]

$$W(x, r) = \frac{\frac{\delta_x \delta_r \sin\left(\frac{\pi x}{\delta_x}\right) \sin\left(\frac{\pi r}{\delta_r}\right)}{x r}}{\iint \frac{\delta_x \delta_r \sin\left(\frac{\pi x}{\delta_x}\right) \sin\left(\frac{\pi r}{\delta_r}\right)}{x r} dx dr} \quad (3.9)$$

with δ_x the azimuth resolution and δ_r the range resolution (m).

By assuming that N_v , σ_b and σ_e are constant inside each tree crown, and have the same value for all crowns in the forest, two new parameters can be identified. The first is the volume backscattering coefficient σ_v

$$\sigma_v = N_v \sigma_b \quad (3.10)$$

and the second is the extinction coefficient

$$\alpha = N_v \sigma_e. \quad (3.11)$$

The forest is thus described by the two parameters, σ_v and α , and by the structure function $S(x, y, z)$. The most prominent fluctuations in the mean images $\langle E_1 \rangle$ and $\langle E_2 \rangle$ are caused by $S(x, y, z)$: individual trees appear locally bright and cast shadows (a small scale effect). However, both short and longer range variations in brightness are caused by α (extinction inside a single crown volume causes *self shading*). Finally, σ_v is a multiplicative factor that can raise or lower the reflectivity of the entire scene. The measures that will be used to compare observed with simulated data will be chosen to be independent of σ_v because the Dornier SAR intensity data are not absolutely calibrated.

3.3 Simulation procedure

It is difficult to obtain experimental measurements of α . Hoekman [21] measured the total two-way extinction at X-band for an oak stand with small gaps $< 1 \text{ m}^2$.

The corresponding range for the one-way extinction α was between 0.12 m^{-1} and 0.15 m^{-1} . Due to the different tree crown structure of most tropical trees when compared to trees in temperate regions, one lower value ($\alpha = 0.075 \text{ m}^{-1}$) and one higher value ($\alpha = 0.3 \text{ m}^{-1}$) will be considered here.

Another concern are the two noise terms $\sqrt{K_n}n_1$ and $\sqrt{K_n}n_2$. The phases $\arg(n_1)$ and $\arg(n_2)$ are assumed to be independent with a uniform pdf. The mean noise power is assumed the same for both antennas and is derived from the observed image data as

$$K_n \langle |n|^2 \rangle = \langle \sigma^0(x, r) \rangle \frac{\langle |E_{\text{shadow}}|^2 \rangle}{\langle |E_{\text{forest}}|^2 \rangle - \langle |E_{\text{shadow}}|^2 \rangle} \quad (3.12)$$

where

$$\sigma^0(x, r) = \left(\int |a(x, y, z)|^2 r d\theta \right) \otimes |W(x, r)|^2. \quad (3.13)$$

The spatial averages $\langle |E_{\text{forest}}|^2 \rangle$ and $\langle |E_{\text{shadow}}|^2 \rangle$ are calculated respectively in an image region containing dense forest and in an image region containing radar shadow caused by the presence of a high mountain. It is well known that $K_n |n|^2$ strongly depends on range distance. The averages are therefore measured at approximately the same range distance as the experimental study site. The simulation procedure can now be summarized by the following steps:

1. Calculate forest structure function $S(x, y, z)$ from field measurements
2. Select a value for α and set σ_v to an arbitrary positive value
3. Draw ϕ_s in $\Delta x \Delta y \Delta z$ from a uniform density $(-\pi, \pi)$ when $S(x, y, z) = 1$
4. Calculate ϕ_1 and ϕ_2 using (3.5) and (3.6)
5. Substitute (3.10) and (3.11) in (3.3) and calculate $a(x, y, z)$
6. Draw $\arg(n_1)$ and $\arg(n_2)$ from a uniform density $(-\pi, \pi)$
7. Assume $K_s = 1$ and calculate $K_n |n|^2$ using (3.12)
8. Calculate $\sqrt{K_n}n_1$ and $\sqrt{K_n}n_2$
9. Evaluate 3.1 and 3.2 resulting in the complex images E_1 and E_2
10. Calculate the L -look InSAR images $\hat{I}_1, \hat{I}_2, \arg \hat{\rho}$ and $|\hat{\rho}|$ by repeating steps 3 to 9 L times.

The above procedure generates a single realisation of L -look InSAR data. The numerical approach presented has the advantage that it can be adapted easily to incorporate processes other than random position fluctuations. For instance, scatterer number density fluctuations could be modelled.

The remainder of this thesis does not require σ^0 -calibration of the intensity data. However, in future this might be desirable, in which case, σ_v needs to be determined by making additional assumptions. A simple additional assumption would be that for optically thick forest, the mean backscatter over the whole scene is independent of $S(x, y, z)$ and α . This assumption has been confirmed for tropical rain forest where the mean value for $\gamma = \sigma^0 / \cos \theta$ typically ranges only from 0.199 (-7.0 dB) to 0.229 (-6.4 dB) and over a whole year [41]. Independence of $S(x, y, z)$ can be understood from the fact that tropical forest vegetation layers have a large thickness (or height). When layer thickness $d \rightarrow \infty$ the water cloud model predicts that [3, equation 6]

$$\gamma_{d \rightarrow \infty} = \frac{\sigma_b}{2\sigma_e}. \quad (3.14)$$

Making the above assumption and a calibrated α , the simulation procedure can be used to calculate calibrated σ^0 -images for any function $S(x, y, z)$.

3.4 Method for comparing observed with simulated data

The location of the simulated InSAR images relative to the observed InSAR images was estimated by registration. The simulated image was translated over the observed image pixel by pixel in azimuth and range direction. For each pixel offset, the linear correlation coefficient between the observed amplitude image and simulated mean amplitude image was calculated as a measure of fit.

After registration, it is in principle possible to compare observed and simulated data on a pixel by pixel basis. For instance, after subtracting a simulated image from an observed image, no structure should be visible in the resulting difference image. However, in practice the above image subtraction method reveals crown geometry measurement errors which makes this method useless for the purpose of validating the scattering model. The crown geometry measurement errors can exceed 10 m in some cases but are assumed to be randomly distributed over the measured forest area. Note that a 10 m error is large compared to the radar range

resolution of 1.25 m and to the average crown dimension.

Because of these problems, a different, statistical approach is taken here. It seems reasonable to assume that the field measurements are statistically unbiased estimates of the true field parameters at the time of data acquisition. So, the statistics of simulated and observed images should therefore be the same. The question remains what measures should be used for comparison. Preferably, these measures should be highly dependent on $S(x, y, z)$ and α .

A suitable measure for the intensity images is the normalised second moment which is calculated from the image of \hat{I} as:

$$I^{(2)} \equiv \frac{\langle \hat{I}^2 \rangle}{\langle \hat{I} \rangle^2}. \quad (3.15)$$

It can be shown that $I^{(2)}$ is directly proportional to α . (See also the theoretical study by Williams [40]).

As a second measure, the mean image coherence magnitude $\langle |\rho| \rangle$ is used because it is inversely proportional to the height variation of scatterers. Due to the irregular nature of $S(x, y, z)$ (see also Fig. 3.1), $\langle |\rho| \rangle$ is expected to be mainly determined by $S(x, y, z)$, and to a lesser extent by α .

As a third measure, the histograms of $|\rho|$ are compared. The shape of the histograms could point to detailed modelling errors not noticed using the other measures.

The autocorrelation of $|\rho|$ in range direction is used as a fourth measure as it is expected to be sensitive to α . The autocorrelation is calculated by averaging individual autocorrelation functions of several azimuth lines.

3.5 Experimental

3.5.1 InSAR data

Two InSAR tracks were used in this study. The first is X-band track Kal.15A, second is C-band track Kal.17A. Both were acquired from near identical view directions (less than 0.001 radian angular difference) and at near identical range and altitude. Since the acquisition geometry is comparable, any differences in image characteristics can be attributed to other system parameters such as frequency, resolution, noise level and baseline. Kal.17A was in zero-Doppler geometry; Kal.15A

was in squinted geometry. Values for $\langle |E_{\text{forest}}|^2 \rangle$ and $\langle |E_{\text{shadow}}|^2 \rangle$ were obtained for both images.

3.5.2 Field measurements

Detailed field measurements were made to calculate $S(x, y, z)$. The positions of 1064 tree crowns in an area of 300 m \times 240 m were measured using a clinometer. These measurements were made approximately three years after the radar data had been acquired. During this period the forest structure will have changed locally, depending on tree species and light condition. Positions of crown top, crown bottom, and of 8 points on the periphery were also measured. Points on the periphery were connected with crown top and bottom using quarter ellipses. The result is a set of two-dimensional closed and piecewise smooth surfaces. Note that crown asymmetry is well preserved by the measurement procedure. Note also that two or more crowns can intersect. Scattering from the ground surface and from tree trunks is ignored. However, *an undergrowth vegetation layer with thickness of 5 m is accounted for*. The z -coordinate of the intersection of tree stem and ground was interpolated (bilinear). The undergrowth vegetation layer was then positioned on top of the ground surface. Fig. 3.1 depicts yz -planes at arbitrarily chosen x -positions in the three-dimensional binary forest structure function $S(x, y, z)$.

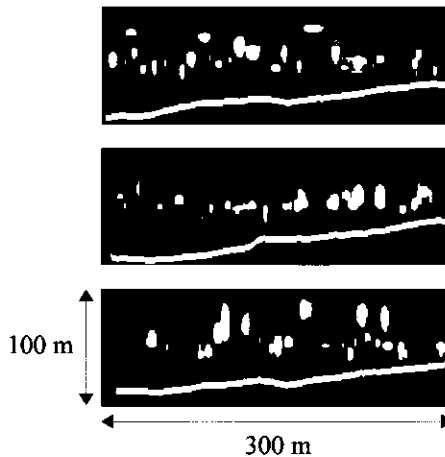


Figure 3.1: yz -planes at arbitrarily chosen x -positions in the three-dimensional binary forest structure function $S(x, y, z)$.

3.6 Results and discussion

For qualitative comparison, image scaling will be consistent for simulated images. In particular, the average intensity is always set to -7 dB. The intensity is displayed on a decibel scale and ranges from -30 dB (black) to 10 dB (white). The phase difference images are not calibrated which means that they have an arbitrary phase offset. Each time the phases are displayed on a linear scale from $-\pi$ to π . Finally, the coherence magnitude is displayed on a linear scale from 0.0 to 1.0.

Simulated X-band and C-band images for $\alpha = 0.15 \text{ m}^{-1}$ are depicted in Fig. 3.2 and Fig. 3.3. Registration for the selection of the corresponding subset from

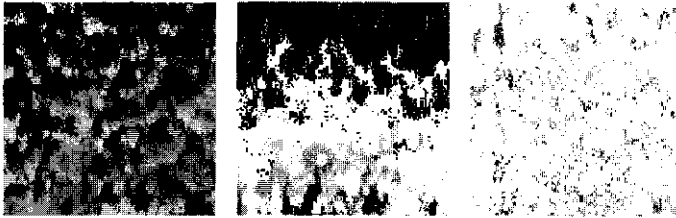


Figure 3.2: Simulated *X-band* intensity, phase difference and coherence magnitude. The images consist of 133 lines (horizontal) by 120 4-look pixels (vertical).

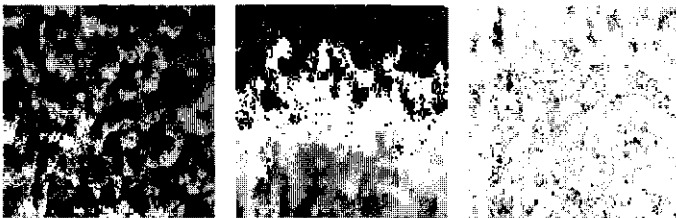


Figure 3.3: Simulated *C-band* intensity, phase difference and coherence magnitude. The images consist of 120 lines (horizontal) by 120 4-look pixels (vertical).

the observed images was done only once using the intensity image and for $\alpha = 0.15 \text{ m}^{-1}$. As can be seen from Fig. 3.2 and Fig. 3.3, *no single structural feature dominates, which means that registration will have to rely on the exact locations of trees (the quality of fieldwork).*

Fig. 3.4 shows the correlation coefficient as a function of azimuth and range translation. Both for X-band and for C-band a clear global maximum can be



Figure 3.4: Correlation coefficient as a function of azimuth and range translation for *X-band* (left) and *C-band* (right). A clear global maximum can be identified in both correlation images (white dot). The size of both images is 130 lines (horizontal) by 130 pixels (vertical).

identified. Fig. 3.5 and Fig. 3.6 show the rectangular subsets of observed InSAR data extracted with the registration procedure. It is immediately clear that the

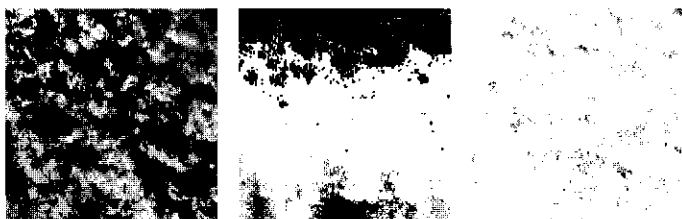


Figure 3.5: Observed *X-band* intensity, phase difference and coherence magnitude. The images consist of 133 lines (horizontal) by 120 4-look pixels (vertical).

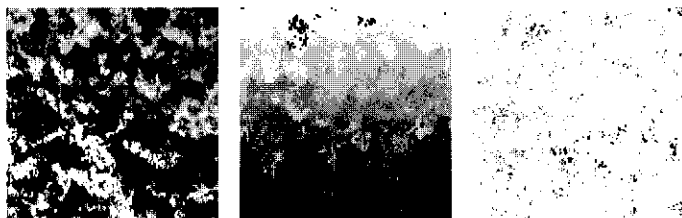


Figure 3.6: Observed *C-band* intensity, phase difference and coherence magnitude. The images consist of 120 lines (horizontal) by 120 4-look pixels (vertical).

observed images are locally very different from the simulated images. However, the overall structure corresponds quite well (i.e. visually).

Table 3.1 compares the simulated and observed $I^{(2)}$ and $\langle |\rho| \rangle$ for X-band. As expected, the value for $I^{(2)}$ is proportional to α . However, none of the sim-

Table 3.1: Normalised second intensity moment $I^{(2)}$ and mean coherence magnitude $\langle|\rho|\rangle$ for observed and simulated *X-band* data with varying extinction coefficient α . The number of pixels $N = 15960$.

Image	$I^{(2)}$	$\langle \rho \rangle$
Observed	3.446	0.942
Simulated: $\alpha = 0.075$	1.837	0.899
Simulated: $\alpha = 0.15$	2.250	0.902
Simulated: $\alpha = 0.3$	2.733	0.890

ulated values is as high as the observed value. The true extinction coefficient must be larger than $\alpha = 0.3 \text{ m}^{-1}$, or alternatively, the physical model (including $S(x, y, z)$) is wrong. The simulated mean coherence magnitude underestimates the experimental value by about 0.04. This is a large difference.

Table 3.2 compares the simulated and observed $I^{(2)}$ and $\langle|\rho|\rangle$ for *C-band*. The

Table 3.2: Normalised second intensity moment $I^{(2)}$ and mean coherence magnitude $\langle|\rho|\rangle$ for observed and simulated *C-band* data with varying extinction coefficient α . The number of pixels $N = 14400$.

Image	$I^{(2)}$	$\langle \rho \rangle$
Observed	2.627	0.889
Simulated: $\alpha = 0.075$	1.887	0.880
Simulated: $\alpha = 0.15$	2.291	0.886
Simulated: $\alpha = 0.3$	2.757	0.878

simulated values for $I^{(2)}$ correspond well with observed values and indicate that α is slightly less than $\alpha = 0.3 \text{ m}^{-1}$. Contrary to the X-band results, all simulated values for $\langle|\rho|\rangle$ now lie close to the observed value, indicating that at least for C-band modelling assumptions (including $S(x, y, z)$) are correct.

Fig. 3.7 and Fig. 3.8 show X-, and C-band histograms of the observed and simulated $|\rho|$. Fig. 3.7 illustrates that the underestimation of $\langle|\rho|\rangle$ at X-band is mainly caused by an underestimation of frequency in the highest interval (0.95, 1.0). Turning to Fig. 3.8, it can be seen that the same effect explains the large difference between X-band $\langle|\rho|\rangle$, and C-band $\langle|\rho|\rangle$. A possible explanation is that X-band scatterers are concentrated in the upper part of the crown and C-band scatterers all over the crown. X-band scattering could originate mainly from a very thin crown

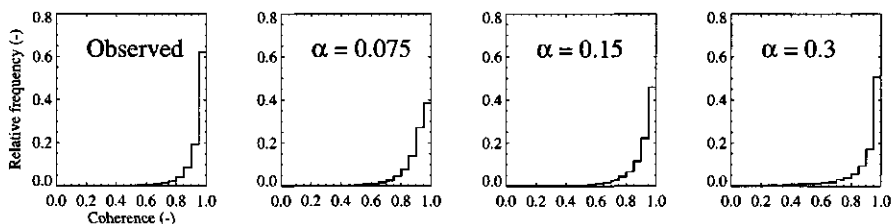


Figure 3.7: Histograms for *X-band* observed and simulated $|\rho|$, as dependent on extinction coefficient α .

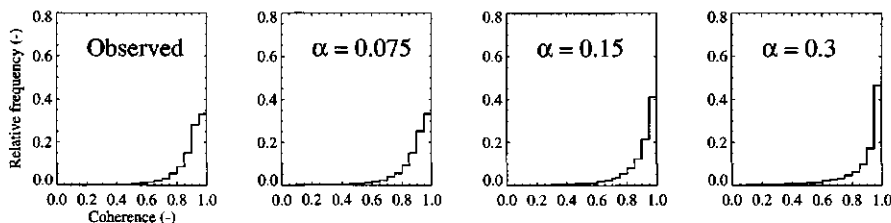


Figure 3.8: Histograms for *C-band* observed and simulated $|\rho|$, as dependent on extinction coefficient α .

top layer. Or, at X-band, $S(x, y, z)$ as measured and modelled gives too much weight to scatterers in the lower part of a crown, resulting in an underestimation of $\langle |\rho| \rangle$.

It must be noted that an additional cause for a differing $\langle |\rho| \rangle$ between X-, and C-band could be a differing number of independent looks. Nominally, $L = 4$ looks was used in the simulation procedure. However, the number of independent looks is a function of SAR system parameters of which not all are at our disposal. There is a way to measure the number of independent looks from the coherence image. In shadow areas the true coherence magnitude must be zero assuming that the noise signals of the two antennas are uncorrelated. The coherence in shadow areas is therefore only dependent on the number of looks. For X-band the observed coherence in the shadow region was 0.489 and for C-band 0.451. Thus, a difference of 0.038 between X- and C-band would be found if all pixels in the image were shadow pixels. Since only a small fraction of the image consists of pure shadow, it can be concluded that a differing number of looks cannot explain the large observed coherence difference between X- and C-band, thereby making the

X-band scattering mechanism assumption more reliable.

Fig. 3.9 shows X- and C-band autocorrelation functions for the observed and simulated $|\rho|$. The extinction coefficient has a profound effect on the autocorrela-

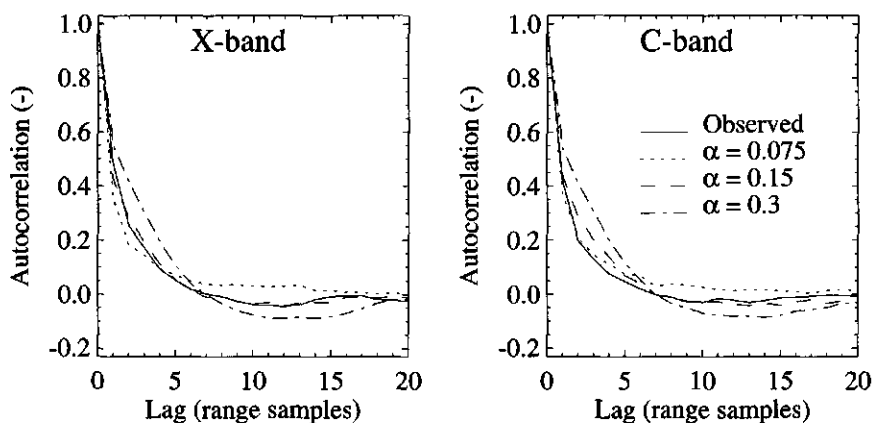


Figure 3.9: Autocorrelation functions of observed and simulated $|\rho|$ for X-, and C-band as dependent on extinction coefficient α .

tion function. Both for X-band and for C-band, $\alpha = 0.15 \text{ m}^{-1}$ best explains the data. This is in contradiction with $I^{(2)}$ which pointed to a larger α .

3.7 Conclusions

The physical assumptions appear to be better at C-band than at X-band. The isotropic uniform crown volume bounded by the outer leaves and branches is possibly incorrect at X-band. Forest structure function $S(x, y, z)$ gives in that case too much weight to the lower crown region.

An extinction coefficient $0.15 < \alpha < 0.3 \text{ m}^{-1}$ seems a reasonable choice at C-band. Two different possible explanations of the observed difference between X-band and C-band mean coherence magnitude have been discussed. It seems that the differing number of independent looks cannot explain the difference, leaving the other explanation related to the differing scattering mechanisms between X- and C-band.

The objective of this Chapter was to assess the validity of the InSAR image

simulation approach as a tool for testing tree map inversion algorithms and as a tool for comparing system designs for tree mapping. For this purpose, and at C-band, the simulations seem accurate enough. For X-band more research is needed.

Chapter 4

Canopy reconstruction theory

4.1 Introduction

This Chapter introduces a theory for forest canopy reconstruction, i.e. the detection of tree crowns and the estimation of crown (x, y, z) -position, size and shape from InSAR images. This inverse problem is ill-posed due to the lack of information, caused by lay-over, radar shadow, speckle and noise. Inversion methods are expected to work well for forest stands over flat terrain. However, serious problems are expected for logged over forest and for forest on hilly terrain. In lay-over regions, tree crown detection and parameter estimation is difficult because different tree crowns are mapped into the same image region. The larger vertical variation of vegetation scatterers increases the width of the phase difference probability density function (pdf), thereby decreasing the accuracy of the crown y - and z -coordinate estimation. The effect of radar shadow is obvious: no tree crowns are detected in shadowed regions. An earlier developed method [39] used the gradient of the interferometric height image to estimate the crown boundary from which crown (x, y, z) -positions were estimated. A disadvantage of that method is that it does not specifically account for extinction, imaging and speckle. In fact, another (ad-hoc) computer vision method could work as well or even better. There is clearly a need for a physical basis from which inversion methods may be developed. *This Chapter therefore focuses on a theory that uses the extended cloud model as starting point and derives expressions for the inverse problem.*

4.2 Data probability density functions

As a starting point it is assumed that the InSAR provides four basic data types. Antenna 1 provides a multi-look estimate $\hat{\sigma}_1$ of the radar cross section σ_1 . Antenna 2 provides, from a slightly different position, a multi-look estimate $\hat{\sigma}_2$ of the radar cross section σ_2 . Finally, the raw data from antennas 1 and 2 are combined to calculate an estimate $\hat{\rho}$ of the complex coherence ρ (complex interferogram). Because the radar resolution is much larger than the size of an individual scatterer, images of the estimates $\hat{\sigma}_1$, $\hat{\sigma}_2$, $\arg \hat{\rho}$ and $|\hat{\rho}|$ have a *noiselike* appearance known as speckle. Knowledge of the probability density function (pdf) of these random variables is essential to do canopy reconstruction in a statistically optimal way. Analytical expressions for the relevant pdf's have been reported in literature [35] and are based on the assumption that the raw data E_1 and E_2 have a circular Gaussian pdf. It can be shown that the L -look estimate $\hat{\sigma}$ in this case obeys a gamma pdf:

$$f(\hat{\sigma}) = \frac{1}{\Gamma(L)} \left(\frac{L}{\sigma}\right)^L \hat{\sigma}^{L-1} e^{-\frac{L\hat{\sigma}}{\sigma}} \quad \hat{\sigma} \geq 0. \quad (4.1)$$

Marginal pdf's of $\arg \hat{\rho}$ and $|\hat{\rho}|$ have also been derived using these assumptions [35]. The expressions for $f(\arg \hat{\rho})$ and $f(|\hat{\rho}|)$ are quite complicated and therefore not attractive for inversion purposes. A solution to this problem is to use the mean cross product $\hat{C} \equiv \langle E_1 E_2^* \rangle$ instead of the complex interferogram $\hat{\rho}$:

$$\hat{C} = \hat{\rho} \sqrt{\hat{\sigma}_1 \hat{\sigma}_2}. \quad (4.2)$$

The joint pdf of $\hat{\sigma}_1$, $\hat{\sigma}_2$, $\arg \hat{C}$, and $|\hat{C}|$ has a simple form often referred to as the *complex Wishart distribution* [36, equation 66]

$$f(\hat{\sigma}_1, \hat{\sigma}_2, |\hat{C}|, \arg \hat{C}) = \frac{L^{2L} \left(\hat{\sigma}_1 \hat{\sigma}_2 - |\hat{C}|^2 \right)^{L-2}}{\pi \Gamma(L) \Gamma(L-1) (\sigma^2 (1 - |\rho|^2))^L} \exp \left(-L \frac{\hat{\sigma}_1 + \hat{\sigma}_2 - 2 |\hat{C}| \cos(\arg \hat{C} - \arg \rho)}{\sigma (1 - |\rho|^2)} \right). \quad (4.3)$$

It has been assumed that $\sigma_1 = \sigma_2 \equiv \sigma$ which is reasonable for a single-pass across track InSAR.

4.3 Simulated templates

Template matching [10] is a standard method to decide if a given object is present at a certain image location (i, j) where i denotes the azimuth pixel number and j denotes the range pixel number. Simulated InSAR templates can be used to determine the presence of tree crowns and to estimate the position (i_0, j_0) and shape of tree crowns. The simulation method developed in Chapter 3 allows for the construction of the templates σ^{temp} , $\arg \rho^{\text{temp}}$ and $|\rho^{\text{temp}}|$ with given microwave extinction coefficient α and a vector \mathbf{s} with crown shape parameters. To complete the geometry, the crown shape can be placed above a horizontal flat scattering layer representing the ground. This has the effect that a steep gradient occurs in all templates at the crown-ground boundary. The scattering geometry thus created, serves as an *average* geometry. Many crown shapes deviate from a symmetric analytical shape such as a sphere or an ellipsoid. Moreover, partly shadowing can result in a highly non-linear deviations in the observed image. One would be tempted to use complicated shapes and describe image deformations caused by shadowing. However, this will increase parameter estimation errors because purely random fluctuations in the data start to dominate the solution. The ellipsoid is a suitable low dimensional shape. Fig. 4.1 shows the template region and template images of σ , $\arg \rho$ and $|\rho|$ using the system parameters: $\lambda = 0.0566$ m, $H = 3000$ m, $B_y = 1$ m, $B_z = 1$ m, $\delta_x = 1$ m and $\delta_r = 1$ m, $\theta = 45^\circ$ and assuming $\alpha = 0.3$ m $^{-1}$. The shape and size of the template region is always chosen to be 1 m larger than the largest shape dimension.



Figure 4.1: From left to right: template region, radar cross section template, phase difference template and coherence magnitude template.

4.4 Likelihood ratio image transform

Given the theoretical pdf's and the model templates, an optimal goodness-of-fit criterion can be defined. Consider first a single pixel at location (i, j) . The goodness-of-fit of parameter $\sigma_{i,j}$ with the observed $\hat{\sigma}_{i,j}$ as a function of the crown parameters can be expressed as the conditional density or likelihood

$$f(\hat{\sigma}_{i,j} | i_0, j_0, \mathbf{s}) = f(\hat{\sigma}_{i,j} | \sigma_{i-i_0, j-j_0}^{\text{temp}}(\mathbf{s})). \quad (4.4)$$

This expression forms the basis for the goodness-of-fit of an entire shape as projected in a certain image region. Let R denote the image region or subset of pixels (i, j) that is covered when a crown with parameters i_0, j_0 and \mathbf{s} is present. Clearly, R is a function

$$R \equiv R(i_0, j_0, \mathbf{s}). \quad (4.5)$$

Depending on the crown shape, the number of pixels N in subset R is variable and also a function

$$N = N(\mathbf{s}). \quad (4.6)$$

The goodness-of-fit of a crown with parameters i_0, j_0, \mathbf{s} can now be derived and will be explained below. Assuming that all pixel values inside the template are conditionally independent, the joint pdf of the N random variables conditional on crown image position i_0, j_0 and crown shape \mathbf{s} is

$$f(\hat{\sigma}_1, \dots, \hat{\sigma}_N | i_0, j_0, \mathbf{s}) = \prod_{i,j \in R} f(\hat{\sigma}_{i,j} | \sigma_{i-i_0, j-j_0}^{\text{temp}}(\mathbf{s})). \quad (4.7)$$

A large value of $f(\hat{\sigma}_1, \dots, \hat{\sigma}_N | i_0, j_0, \mathbf{s})$ must be interpreted as a large probability that a crown with shape vector \mathbf{s} is present at image position (i_0, j_0) . However, to determine whether this crown is actually present at image region R , it is necessary to test against an alternative hypothesis for region R . A suitable alternative hypothesis is that the data $\hat{\sigma}_1, \dots, \hat{\sigma}_N$ are consistent with a horizontal ground surface geometry with radar cross section σ_g and joint conditional density

$$f(\hat{\sigma}_1, \dots, \hat{\sigma}_N | i_0, j_0, \sigma_g, \mathbf{s}) = \prod_{i,j \in R} f(\hat{\sigma}_{i,j} | \sigma_g). \quad (4.8)$$

Using the maximum likelihood criterion [13] and the gamma pdf in (4.1), a shape with vector \mathbf{s} is declared present if

$$\frac{\prod_{i,j \in R} f(\hat{\sigma}_{i,j} | \sigma_{i-i_0, j-j_0}^{\text{temp}}(\mathbf{s}))}{\prod_{i,j \in R} f(\hat{\sigma}_{i,j} | \sigma_g)} > 1. \quad (4.9)$$

Taking the natural logarithm on both sides and simplifying the result gives

$$\underbrace{\sum_{i,j \in R} \hat{\sigma}_{i,j} \left(\frac{1}{\sigma_g} - \frac{1}{\sigma_{i-i_0, j-j_0}^{\text{temp}}(s)} \right)}_{\text{Linear image transform}} + \underbrace{N \ln \sigma_g - \sum \ln \sigma^{\text{temp}}(s)}_{\text{Template dependent term}} > 0. \quad (4.10)$$

The left hand side of this expression consists of a linear image transform plus a template dependent term. The entire operation is a linear transform of the radar cross section image $\hat{\sigma}$ and a function of object parameters i_0, j_0 and s . This transform will be denoted as $H_{\hat{\sigma}}(i_0, j_0, s)$. In practice the shape parameter space is first made discrete, for instance resulting in 10 different shapes. The linear image transform in (4.10) must then be evaluated 10 times for each template location (i_0, j_0) whereas the template dependent term is only evaluated 10 times. The entire operation is done using spatial filtering. However, when applying the convolution Theorem, the linear filter could be calculated efficiently with the Fast Fourier Transform [29, p.538].

The question now arises whether a simple result as in (4.10) can be obtained when all observed data $(\hat{\sigma}_1, \hat{\sigma}_2 \text{ and } \hat{C})$ are used simultaneously. Using again the maximum likelihood criterion a shape with vector s and image location (i_0, j_0) is declared present if

$$\frac{\prod_{i,j \in R} f\left(\hat{\sigma}_{1,i,j}, \hat{\sigma}_{2,i,j}, \left|\hat{C}_{i,j}\right|, \arg \hat{C}_{i,j} \left| \sigma_{i-i_0, j-j_0}^{\text{temp}}(s) \right|, \left| \rho_{i-i_0, j-j_0}^{\text{temp}}(s) \right|, \arg \rho_{i-i_0, j-j_0}^{\text{temp}}(s)\right)}{\prod_{i,j \in R} f\left(\hat{\sigma}_{1,i,j}, \hat{\sigma}_{2,i,j}, \left|\hat{C}_{i,j}\right|, \arg \hat{C}_{i,j} \left| \sigma_g \right|, \left| \rho_g \right|, \arg \rho_g\right)} > 1. \quad (4.11)$$

Taking the natural logarithm on both sides and simplifying the result gives

$$\begin{aligned} & \underbrace{\sum_{i,j \in R} \frac{\hat{\sigma}_{1,i,j} + \hat{\sigma}_{2,i,j} - 2 \left| \hat{C}_{i,j} \right| \cos \left(\arg \hat{C}_{i,j} - \arg \rho_g \right)}{\sigma_g (1 - |\rho_g|^2)}}_{\text{Non-linear image transform}} \\ & - \underbrace{\sum_{i,j \in R} \frac{\hat{\sigma}_{1,i,j} + \hat{\sigma}_{2,i,j} - 2 \left| \hat{C}_{i,j} \right| \cos \left(\arg \hat{C}_{i,j} - \arg \rho_g^{\text{temp}} \right)}{\sigma_{i-i_0, j-j_0}^{\text{temp}} \left(1 - \left| \rho_{i-i_0, j-j_0}^{\text{temp}} \right|^2 \right)}}_{\text{Non-linear image transform}} \\ & + \underbrace{\sum \ln (\sigma_g)^2 (1 - |\rho_g|^2) - \sum \ln (\sigma^{\text{temp}})^2 \left(1 - \left| \rho_g^{\text{temp}} \right|^2 \right)}_{\text{Template dependent term}} > 0. \quad (4.12) \end{aligned}$$

This transform will be denoted as $H_{\hat{\sigma}_1, \hat{\sigma}_2, \hat{C}}(i_0, j_0, s)$. The transform operates on all available image data (four real numbers per pixel) and is again a function of object

parameters i_0, j_0 and s . However, there is a problem with this transform. *The difficulty lies in the fact that the height of a tree crown is not known a-priori*, which means that phase difference estimates of the crown and the ground are required at every pixel position. This can be done using maximum likelihood estimation. An analysis of the trade-off between computational efficiency ($H_{\hat{\sigma}}(i_0, j_0, s)$) and possibly more accurate parameter estimates ($H_{\hat{\sigma}_1, \hat{\sigma}_2, \hat{C}}(i_0, j_0, s)$) is outside the scope of this thesis. The next Chapter will therefore focus on the transform $H_{\hat{\sigma}}(i_0, j_0, s)$ in equation (4.10), which is fast and straightforward.

4.5 Solution to the multiple response problem

In the field of pattern recognition it has long been known that under noisy conditions, multiple response (multiple matches) will occur close to the true object location [10, p.283], [24]. Consider for instance the case where two template matches occur for two tree crowns that overlap in 3D space. Formally, this situation could be avoided by incorporating non-independent probabilities for crown 3D locations using stochastic prior interaction models. Such a theory was formulated in [24] using nearest-neighbour Markov point processes. A solution must then be found iteratively by successive updates of position and shape parameters. However, a simpler solution can be obtained through a local analysis of the transforms $H_{\hat{\sigma}}(i_0, j_0, s)$ or $H_{\hat{\sigma}_1, \hat{\sigma}_2, \hat{C}}(i_0, j_0, s)$. The problem of multiple response means that there are at least two competing solutions, each of which excludes the other as an acceptable solution. Only one must be selected, and a natural choice is to select the shape for which $H_{\hat{\sigma}}(i_0, j_0, s)$ or $H_{\hat{\sigma}_1, \hat{\sigma}_2, \hat{C}}(i_0, j_0, s)$ is largest. What remains is to define when shapes lie too close to each other. A useful measure is the distance between the shape centre points as measured in image space (x, r) . This distance may not be too small since this would mean that the two shapes would occupy the same image space, a situation which is physically feasible, but very unlikely to result in good parameter estimates for both shapes. (Refer to the lay-over problem in Chapter 2). The distance can for instance be chosen to be larger than the smallest shape dimension (which is 3 m in most practical cases). Valid points in $H_{\hat{\sigma}}(i_0, j_0, s)$ or $H_{\hat{\sigma}_1, \hat{\sigma}_2, \hat{C}}(i_0, j_0, s)$ can now be selected using a simple local filtering operation.

4.6 Phase unwrapping and position calculation

The previous filtering operation results in a subset of the transform $H_{\hat{\sigma}}(i_0, j_0, \mathbf{s})$ or $H_{\hat{\sigma}_1, \hat{\sigma}_2, \hat{C}}(i_0, j_0, \mathbf{s})$ representing crowns with varying (i_0, j_0) -image position and shape \mathbf{s} . What remains is estimates of y - and z -coordinate of the crown centre point (y_0, z_0) fixing the shape in 3D space. Both coordinates follow from the unwrapped phase difference $\phi_{0,u}$ of the shape centre point (x_0, y_0, z_0) . An estimate of the wrapped phase difference $\phi_{0,w}$ can be obtained from the average cross-product over the template region R :

$$\hat{\phi}_{0,w} = \arg \sum_{i,j \in R} \hat{C}_{i,j}. \quad (4.13)$$

where the wrapped phase estimate $\hat{\phi}_{0,w}$ is related to the unwrapped phase estimate $\hat{\phi}_{0,u}$ by the relation

$$\hat{\phi}_{0,w} = \left(\left(\hat{\phi}_{0,u} + \pi \right) \bmod 2\pi \right) - \pi. \quad (4.14)$$

The unwrapped phase $\hat{\phi}_{0,u}$ can be obtained from this equation using the necessary assumption that the change of $\phi_{0,u}$ between two crowns lying close to each other in image space is always less than 2π . Using this assumption, $\hat{\phi}_{0,w}$ can be unwrapped using a method similar to the methods described in [4]. Finally, assuming linear and parallel flight tracks, the shape centre point (x_0, y_0, z_0) follows from ϕ_0 , i_0 , j_0 and the range to the first pixel as expressed in (B.1), (B.2) and (B.3).

4.7 Combining orthogonal tracks

Use of orthogonal tracks (different illumination directions) could improve reconstruction in regions with lay-over or shadow where the reconstruction is problematic in one data set but not in the other and visa versa. However, combining two data sources introduces additional problems. For instance, the two separate solutions can be locally *inconsistent*, and one has to choose one of the two solutions or alternatively a new solution that is an *average* of each separate solution. A further problem is that the two tracks need to be geometrically aligned or coregistered.

4.8 Conclusions

Both transforms $H_{\hat{\sigma}}(i_0, j_0, \mathbf{s})$ and $H_{\hat{\sigma}_1, \hat{\sigma}_2, \hat{C}}(i_0, j_0, \mathbf{s})$ use the theoretical Gaussian speckle model and simulated template images for optimal canopy reconstruction. The transform $H_{\hat{\sigma}}(i_0, j_0, \mathbf{s})$ is straightforward and easy to implement. Because of its simplicity it will be used in Chapter 5 for comparing the performance of different InSAR system configurations. The transform $H_{\hat{\sigma}_1, \hat{\sigma}_2, \hat{C}}(i_0, j_0, \mathbf{s})$ is much more complicated than the transform $H_{\hat{\sigma}}(i_0, j_0, \mathbf{s})$ and requires for each pixel location the estimation of two additional phases corresponding to the location of scattering for the tree crown and the ground surface. The full exploitation of the complex Wishart distribution by the transform $H_{\hat{\sigma}_1, \hat{\sigma}_2, \hat{C}}(i_0, j_0, \mathbf{s})$ could result in much better tree crown recognition and crown parameter estimation when compared to $H_{\hat{\sigma}}(i_0, j_0, \mathbf{s})$. However, an efficient algorithmic implementation of $H_{\hat{\sigma}_1, \hat{\sigma}_2, \hat{C}}(i_0, j_0, \mathbf{s})$ remains to be defined.

Chapter 5

Effect of system parameters

5.1 Introduction

To study the effect of InSAR system parameters on the quality of inverted tree positions this Chapter applies the simulation method of Chapter 3. The parameters of interest are the total number of detected crowns and crown (x, y, z) -positions. The inversion is based on the transform $H_{\hat{\sigma}}(i_0, j_0, \mathbf{s})$ that was introduced in Chapter 4

5.2 Theory

5.2.1 Effect of baseline length

Baseline length influences the height sensitivity β (rad m^{-1}) of the interferometer. Increasing the effective baseline B_n makes the interferometer more sensitive to the height variation of scatterers. However, increasing B_n decreases the coherence in accordance with the Van Cittert-Zernike Theorem, thereby increasing *random* errors in the y - and z -coordinate. In the limit $B_n \rightarrow \infty$, the y - and z -coordinates become uniform random variables. In the limit $B_n \rightarrow 0$, the SNR will dominate the coherence magnitude and a small random phase error will cause a large error in y and z . It can be concluded that an optimum B_n must exist. The Cramer-Rao bound for the phase standard deviation was shown to be given by [30]

$$\text{std}[\phi] \approx \frac{1}{\sqrt{2L}} \frac{\sqrt{1 - |\rho|^2}}{|\rho|}. \quad (5.1)$$

The standard deviations of y and z are then approximately

$$\text{std}[y] \approx \frac{\text{std}[\phi]}{\beta \tan \theta} \quad (5.2)$$

and

$$\text{std}[z] \approx \frac{\text{std}[\phi]}{\beta}. \quad (5.3)$$

This gives the exact functional dependence of (y, z) -errors on B_n via $|\rho|$. This relation depends strongly on forest 3D structure and can therefore only be determined using numerical simulation. Another concern is the height of ambiguity defined by [4]

$$z_{2\pi} = \frac{r\lambda \sin \theta}{mB_n}. \quad (5.4)$$

When B_n increases, $z_{2\pi}$ decreases, thereby increasing the chance that a crown is reported at a wrong (y, z) -location due to *random* y - and z -errors.

5.2.2 Effect of incidence angle

Incidence angle θ is the only parameter that changes the lay-over geometry. It changes the configuration of scatterers inside the resolution cell. Incidence angle has therefore a strong influence on the geometric decorrelation. Small incidence angles will result in large decorrelation whereas large incidence angles result in small decorrelation. However, large incidence angles will result in an increase in shadowed area.

5.2.3 Effect of thermal noise power

The relative contribution of thermal power $|n|^2$ to intensity $|E|^2$ increases with altitude H as H^3 . Flying high has the advantage that motion compensation errors are smaller because there is often less turbulence at greater altitudes. More important, increasing altitude increases swath width making the system cheaper to operate. It is therefore useful to evaluate the effect of thermal noise on tree map retrieval errors. An increase in $|n|^2$ has two different degrading effects on inverted tree maps. First, an increase in $|n|^2$ decreases intensity contrast making detection more difficult. Second, an increase in $|n|^2$ causes an increase in *random* y and z error via the coherence magnitude. To quantify this second effect, consider a crown with $\text{SNR} = 100$ (20 dB) and zero volume and slant range decorrelation

($|\rho|_{\text{volume}} = |\rho|_{\text{slantrange}} = 1.0$). The noise coherence is $|\rho|_{\text{noise}} = \text{SNR}/(\text{SNR}+1) \approx 0.99$. For a single-look pixel ($L = 1$), a coherence of 0.99 gives $\text{std}[\phi] \approx 0.1$. For an InSAR with $m = 2$, $B_n \approx 1$ m, $\lambda = 0.056$ m, $r = 5000$ m and $\theta = 45^\circ$, the height sensitivity $\beta \approx 0.0635$ rad m⁻¹. The resulting y and z errors are $\text{std}[y] = \text{std}[z] \approx 1.58$ m. These errors are acceptable, since in practice not a single look but more than 100 looks can cover a tree crown. However, since $|\rho|_{\text{volume}}$ will dominate $|\rho|$ for most forests, the errors are expected to be much larger. A realistic value for $|\rho|_{\text{volume}}$ can only be obtained numerically using a realistic 3D model forest and the simulation method.

5.2.4 Effect of number of looks (or resolution)

The number of looks, or resolution, affects both the detection and the position estimates. Detection becomes more difficult when speckle dominates the intensity images. Increasing the number of looks with a given factor also decreases the (y, z) -coordinate errors with approximately the square root of that factor.

Table 5.1: InSAR system configurations that were compared. Baseline z -component B_z , incidence angle θ , number of looks L and Signal to Noise Ratio (SNR).

System	B_z (m)	θ ($^\circ$)	L (-)	SNR (dB)
1	1	50	4	20
2	0.5	50	4	20
3	1.5	50	4	20
4	1	55	4	20
5	1	60	4	20
6	1	50	2	20
7	1	50	8	20
8	1	50	4	15
9	1	50	4	25

5.3 Experimental

Theoretical InSAR images were calculated for nine different InSAR system configurations using a realistic forest geometry containing 50 spheres representing tree crowns. The 50 spheres with a fixed radius of 5 m were placed at a random 3D location above a plane horizontal scattering layer. The z -coordinate of the sphere

centre varied between 10 m and 20 m. The horizontal vegetation layer extended from $z = 0$ m to $z = 1$ m. The following set of system parameters is common to all simulations: $B_y = 0.5$ m, $\lambda = 0.056$ m, $H = 3000$ m and $m = 2$. The remaining system parameters were chosen as small variations around the Dornier SAR system as operated during INDREX-96. Table 5.1 lists the InSAR system configurations that were compared. To calculate the position error, a one-to-one correspondence was established between true and inverted positions. Each true position was matched with only one inverted position using the following procedure. The Euclidian distance $\sqrt{(x - \hat{x})^2 + (y - \hat{y})^2 + (z - \hat{z})^2}$ was computed for all possible pairs of true and estimated positions. Pairs were then selected in order of increasing distance and only if either the true or the estimated position was not already selected.

5.4 Results and discussion

Fig. 5.1 shows true and inverted crown positions for system 1 in Table 5.1 projected onto the xy-plane. A systematic shift towards smaller y -values can be seen. This effect is large when the ground surface is directly illuminated by the radar (lay-over) which is apparent for the crowns closest to the radar. This inversion example also shows that the multiple response problem still occurs in some cases. For instance, a clustering of three inverted crowns is found near to the true crown location of $x \approx 65$ m and $y \approx 3860$ m. Fig. 5.2 shows the simulations of radar cross section $\hat{\sigma}$, interferometric phase $\arg \hat{\rho}$ and coherence magnitude $|\hat{\rho}|$ for the 9 systems in Table 5.1. Although the images look very similar, some differences can be detected by eye. Table 5.2 lists the number of detections and the position errors. As expected there is a systematic bias in the y - and z -coordinate estimate. This bias could be removed with the method outlined in Chapter 2. The differences between systems is small. System 5 performs well since it has a high detection rate plus relatively small mean errors and mean absolute errors in the coordinates.

5.5 Conclusions

In theory, the effect of baseline length B , incidence angle θ , thermal noise $|n|^2$ and number of looks L can be explained. The configuration of crowns in the 3D forest

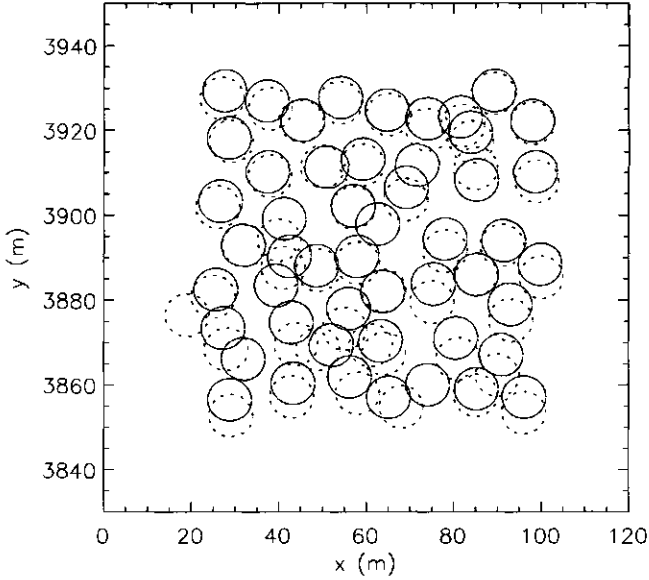


Figure 5.1: True (solid line) and inverted (broken line) crown positions for system 1 projected onto the xy-plane.

Table 5.2: Number of detections N_d , mean errors ($me[x_0]$, $me[y_0]$ and $me[z_0]$) and mean absolute errors ($mae[x_0]$, $mae[y_0]$ and $mae[z_0]$).

System	N_d	$me[x_0]$	$me[y_0]$	$me[z_0]$	$mae[x_0]$	$mae[y_0]$	$mae[z_0]$
1	47	0.3	-3.1	-2.7	2.2	3.6	3.0
2	47	-1.0	-3.7	-2.7	1.8	4.0	2.7
3	47	-0.9	-2.7	-2.4	1.8	3.4	2.6
4	46	0.3	-2.2	-2.6	1.3	3.0	2.9
5	48	1.0	-2.6	-1.9	2.1	2.7	2.5
6	46	-0.5	-2.8	-2.8	1.8	3.6	2.9
7	43	-0.2	-2.3	-2.7	1.0	2.8	2.9
8	47	0.3	-3.1	-2.7	2.2	3.6	3.0
9	47	0.3	-3.1	-2.7	2.2	3.6	3.0

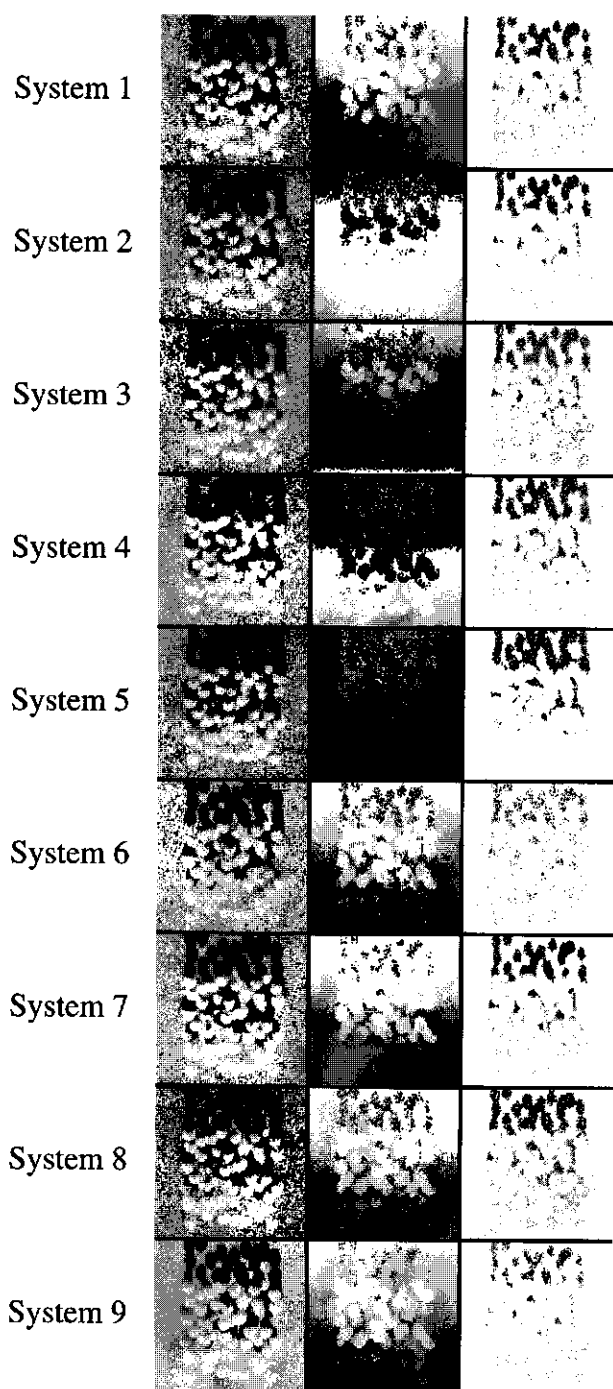


Figure 5.2: Simulations of radar cross section $\hat{\sigma}$, interferometric phase $\arg \hat{\rho}$ and coherence magnitude $|\hat{\rho}|$ for the 9 systems given in Table 5.1. Simulations are of 50 crowns randomly positioned above a flat scattering plane.

structure is however critical in quantifying the magnitude of these effects. Numerical simulations have shown that for the parameter ranges under consideration all 9 systems perform similarly. *This indicates that there is quite some flexibility in operating modes, and also that InSAR's could still operate at low SNR (15 dB) enabling higher resolution, higher altitudes or lower transmit power.*

Chapter 6

Questions and recommendations

In this Chapter, questions are asked about the previous Chapters on the bases of which recommendations for future research are given.

6.1 Is the scattering model appropriate?

The first and second order image statistics used in Chapter 3 for comparing observed with simulated data is not sufficient to decide on the validity of the extended cloud model for a single tree crown. For inversion, it is important to know the spatial pattern of the underlying backscattering amplitude, interferometric phase and coherence magnitude for a single tree crown as a function of crown shape, branch structure and species. *The validation which is now lacking, can be made by flying the same short track many times.* Ten acquisitions will reduce the speckle level sufficiently so that a detailed analysis can be done for a number of interesting geometries (i.e. different tree species, solitary tree, lay-over situation). Preferably these geometries are measured before or during radar data acquisition.

6.2 What are new developments?

Combining two orthogonal InSAR tracks is the most promising method that can solve to a large extent the problems of lay-over and shadow. An open question is whether existing SAR processing methods (such as motion compensation) are sufficiently accurate or not for a successful spatial registration of the two tracks. The INDREX tracks Kal.17A and Kal.18A are well suited for an initial analysis.

Multi-baseline and multi-altitude InSAR add observations with a differing height sensitivity. This could improve the calibration of position correction equations. Multi-baseline InSAR can be operationally attractive because two effective baselines can be made by using only a single physical baseline and processing the signals in two different ways at the expense of resolution.

At high resolution, polarimetry could provide information related to structure and species. Polarimetric interferometry at L- or P-band may yield information on forest height.

6.3 How to proceed?

The assumption of many identical independent random scatterers per resolution cell leading to circular complex Gaussian pdf's for E_1 and E_2 may be violated at higher resolutions. *It is thus recommended that the statistics of C-band InSAR data are studied for these higher resolutions.*

The lack of simultaneous good quality ground truth measurements made the INDREX data unsuitable for validating inversion methods. In this thesis, only simulated images could be used for this purpose. New InSAR experiments directed towards the validation of inversion methods are required. *It seems better to experiment first in European plantation forests.* These are spatially more homogeneous and the logistics are simpler. *Moreover, the theory developed in this thesis may be of interest for operational monitoring of European plantation forest.* However, the theory has been developed for the application in tropical forest where the certification of wood is almost impossible without an effective all-weather monitoring system. *More InSAR experiments with emphasis on timely acquisition of ground truth will therefore be needed in tropical regions on Earth.*

Appendix A

Derivation of equation (2.2)

This derivation of (2.2) is similar to the one given in [42] and [1]. A new coordinate system (ξ, η, ζ) is introduced with origin at expansion point (x, y, z) but rotated $\theta - \pi/2$ with respect to z (*plane wave approximation*) [4, p.R8]

$$\begin{bmatrix} \xi' \\ \eta' \\ \zeta' \end{bmatrix} = \begin{bmatrix} 1 & 0 & 0 \\ 0 & \sin \theta & -\cos \theta \\ 0 & \cos \theta & \sin \theta \end{bmatrix} \begin{bmatrix} x' - x \\ y' - y \\ z' - z \end{bmatrix}. \quad (\text{A.1})$$

Following [17, p. 209] the *paraxial approximation* can be used for the two range distances

$$r'_1 = \sqrt{(r')^2 + \left(\zeta' + \frac{B_n}{2}\right)^2} \approx r' + \frac{(\zeta' + \frac{B_n}{2})^2}{2r'} \quad (\text{A.2})$$

$$r'_2 \approx B_p + \sqrt{(r')^2 + \left(\zeta' - \frac{B_n}{2}\right)^2} \approx B_p + r' + \frac{(\zeta' - \frac{B_n}{2})^2}{2r'} \quad (\text{A.3})$$

where $B_n = B \cos(\theta - \alpha)$ and $B_p = B \sin(\theta - \alpha)$. Relative to the expansion point, the phase difference ϕ is now [4, equation 27]

$$\phi \approx B_p + \frac{2\pi m B_n}{\lambda r} \zeta'. \quad (\text{A.4})$$

Using (A.1) in (A.4) the mean cross-product $\langle E_1 E_2^* \rangle$ becomes ([20], equation 9)

$$\langle E_1 E_2^* \rangle = K_s e^{-i \frac{2\pi m B_p}{\lambda}} \int_V |W(\xi', \eta')|^2 \sigma_v(z') e^{i \frac{2\pi m B_n}{\lambda r} ((y' - y) \cos \theta + (z' - z) \sin \theta)} dV'. \quad (\text{A.5})$$

In arriving at (A.5), it has been assumed that registration of the two complex channels is perfect, and that $\sigma_v(x', y', z') = \sigma_v(z')$. To make progress, a change

of integration variables is needed [23, p.247]. Using (A.1) results in the following transformation

$$\begin{aligned} y' - y &= \frac{\eta' + (z' - z) \cos \theta}{\sin \theta} \\ z' - z &= z' - z. \end{aligned} \quad (\text{A.6})$$

Substitution of (A.6) in the complex exponential term in (A.5) gives

$$\begin{aligned} e^{i \frac{2\pi m B_n}{\lambda r} ((y' - y) \cos \theta + (z' - z) \sin \theta)} &= e^{i \frac{2\pi m B_n}{\lambda r} \left(\frac{\eta' \cos \theta}{\sin \theta} + (z' - z) \frac{\cos^2 \theta}{\sin \theta} + (z' - z) \sin \theta \right)} \\ &= e^{i \frac{2\pi m B_n}{\lambda r \tan \theta} \eta'} e^{i \frac{2\pi m B_n}{\lambda r \sin \theta} z'}. \end{aligned} \quad (\text{A.7})$$

The Jacobian of the transformation in (A.6) is

$$J = \begin{vmatrix} \frac{\partial(y'-y)}{\partial\eta'} & \frac{\partial(y'-y)}{\partial(z'-z)} \\ \frac{\partial(z'-z)}{\partial\eta'} & \frac{\partial(z'-z)}{\partial(z'-z)} \end{vmatrix} = \begin{vmatrix} \frac{1}{\sin \theta} & \frac{\cos \theta}{\sin \theta} \\ 0 & 1 \end{vmatrix} = \frac{1}{\sin \theta}. \quad (\text{A.8})$$

Using (A.7) and (A.8) in (A.5) gives

$$\langle E_1 E_2^* \rangle = K_s \frac{e^{-i \frac{2\pi m B_p}{\lambda}}}{\sin \theta} \int \int |W(\xi', \eta')|^2 e^{i \frac{2\pi m B_n}{\lambda r \tan \theta} \eta'} d\xi' d\eta' \times \int \sigma_v(z') e^{i \frac{2\pi m B_n}{\lambda r \sin \theta} z'} dz'. \quad (\text{A.9})$$

The received intensities are approximately equal due to an almost identical line of sight,

$$\langle E_1 E_1^* \rangle = \langle E_2 E_2^* \rangle = \frac{1}{\sin \theta} \left(K_s \int \sigma_v(z') dz' + K_n |n|^2 \right). \quad (\text{A.10})$$

To arrive at (A.10) it has been assumed that the noise contributions in both channels are approximately equal. Note that the noise terms do not appear in the expressions for $\langle E_1 E_2^* \rangle$ because the complex variables n_1 and n_2 are uncorrelated. The complex coherence is defined [6]

$$\rho = \frac{\langle E_1 E_2^* \rangle}{\sqrt{\langle |E_1|^2 \rangle \langle |E_2|^2 \rangle}}. \quad (\text{A.11})$$

The following derivation has been given in different forms by Zebker and Villasenor [42] and by Askne *et.al.*[1]. Inserting (A.9) and (A.10) in (A.11), the coherence magnitude becomes

$$|\rho| = \frac{K_s \left| \int \int |W(\xi', \eta')|^2 e^{i \frac{2\pi m B_n}{\lambda r \tan \theta} \eta'} d\xi' d\eta' \right| \left| \int \sigma_v(z') e^{i \frac{2\pi m B_n}{\lambda r \sin \theta} z'} dz' \right|}{K_s \int \sigma_v(z') dz' + K_n |n|^2}. \quad (\text{A.12})$$

Multiplying both the numerator and the denominator with $K_s \int \sigma_v(z') dz'$ results in (2.2).

Appendix B

Position of the scattering phase centre

Calculating the position (x, y, z) of the pixel scattering phase centre requires knowledge of various SAR system and SAR processing parameters. Exact and approximate solutions of the *Interferometric Range Doppler Equations* are discussed in [16]. In this thesis the two antennas are assumed to follow linear and parallel tracks. The x -coordinate follows from azimuth pixel number i and azimuth pixel spacing δ_i

$$x = \left(i - \frac{1}{2}\right) \delta_i. \quad (\text{B.1})$$

Using the approximation $r_1 + r_2 \approx 2r$, the y - and z -coordinate follow from the slant range r and the calibrated unwrapped phase difference: ϕ_u as

$$y = r \sin \left(\cos^{-1} \left(\frac{\lambda \phi_u}{2\pi m B} \right) + \tan^{-1} \left(\frac{B_y}{B_z} \right) \right), \quad (\text{B.2})$$

$$z = H - \sqrt{r^2 - y^2}. \quad (\text{B.3})$$

The slant range coordinate r follows from the range to the first pixel, the range pixel number j , and the range pixel spacing δ_j

$$r = \text{range to first pixel} + \left(j - \frac{1}{2}\right) \delta_j. \quad (\text{B.4})$$

Summary

Tree level monitoring of tropical forest is needed to enforce national legislation for sustainable forest management and to verify implementation of guidelines for sustainable forest management as proposed by the International Tropical Timber Organization (ITTO). This thesis investigates the possibilities of InSAR for the retrieval of 3D crown positions.

To study the potential of imaging radar, the Indonesian Radar Experiment (INDREX) campaign was executed in Indonesia on Borneo and Sumatra in 1996 under the auspices of the Indonesian Ministry of Forestry (MOF) and the European Space Agency (ESA).

Chapter 2 concentrates on the radar lay-over problem. The observed coherence as found for emergent trees was compared with predictions using a simple model for the phase coherence. The coherence was modelled using four different functions for the volume backscattering coefficient $\sigma_v(z')$: the symmetric delta function (2.6), the symmetric rectangular function (2.9), the asymmetric delta function (2.12) and the asymmetric rectangular function (2.13). In general, it can be stated that good position corrections for individual trees are possible only when crown shapes are known *a priori* for each tree. In practical situations it may be feasible to adopt an *efficient average* shape, resulting in *optimised* correction equations. Results show that coherence magnitudes of emergent trees can be predicted satisfactory on the basis of field observations and the use of simple models for the vertical distribution of backscattering. It was shown that good results can be obtained when all backscatter is assumed to be originating from horizontal planes located at the top of the emergent tree and at the top of its lay-over region.

Chapter 3 describes an Interferometric SAR image simulation procedure for 3D forest canopies. The procedure may be used to test canopy reconstruction algorithms and to compare different InSAR system configurations for canopy reconstruction. The InSAR simulation model is an extension of the water cloud

model [3] adding interferometric phase and coherence and describing the geometry of each tree crown. Predictions were made for three values of the extinction coefficient α : 0.075 m^{-1} , 0.15 m^{-1} and 0.3 m^{-1} . At X- and C-band, the tree crown was assumed to be an isotropic random scattering volume consisting of many independent scatterers per resolution cell (single scattering). Random fluctuations were introduced by assuming that scatterers have *independent uniform random* (x, y, z) -coordinates. The forest was thus described by the two parameters, σ_v and α and by the binary forest structure function $S(x, y, z)$. Results of the comparison indicate that the isotropic uniform crown volume bounded by the outer leaves and branches is possibly incorrect at X-band. The physical assumptions seem appropriate at C-band indicating that an extinction coefficient $0.15 < \alpha < 0.3 \text{ m}^{-1}$ is quite realistic at this frequency.

Chapter 4 introduces a theory for 3D forest canopy reconstruction from InSAR data. An optimal method is proposed that uses the assumption that the electric fields E_1 and E_2 each obey a complex circular Gaussian probability density function. Simulated templates of crown shapes were then used to optimally locate crowns in the InSAR data. Two likelihood ratio image transforms were derived for this purpose. The transform $H_{\hat{\sigma}}(i_0, j_0, \mathbf{s})$ uses only the radar cross section image to estimate crown location and shape. The transform $H_{\hat{\sigma}_1, \hat{\sigma}_2, \hat{C}}(i_0, j_0, \mathbf{s})$ on the other hand uses in addition interferometric phase and coherence magnitude. The transform $H_{\hat{\sigma}}(i_0, j_0, \mathbf{s})$ has been implemented efficiently whereas the transform $H_{\hat{\sigma}_1, \hat{\sigma}_2, \hat{C}}(i_0, j_0, \mathbf{s})$ will need further study on efficient implementation.

Chapter 5 uses the InSAR image simulation method to study the effect of the system parameters: baseline length, incidence angle, thermal noise power and number of looks. *Results indicate that InSAR's could still operate at low SNR (15 dB) enabling higher resolution, higher altitudes or lower transmit power.*

Samenvatting

Het monitoren van tropisch bos is noodzakelijk voor het naleven van de nationale wetgeving met betrekking tot duurzaam bosbeheer en de controle op het ten uitvoer brengen van richtlijnen, zoals vastgelegd door de International Tropical Timber Organization (ITTO). In dit proefschrift werden de mogelijkheden van de InSAR techniek voor het meten van boomkroon posities in tropisch regenbos onderzocht.

Om de mogelijkheden van 3D-radarbeeldvorming te bestuderen hebben in 1996 het Indonesische Ministerie van Bosbouw (MOF) en de European Space Agency (ESA) het Indonesian Radar Experiment (INDREX) uitgevoerd.

Hoofdstuk 2 is gewijd aan het radar *lay-over* probleem. De waargenomen coherentie is vergeleken met voorspellingen van een eenvoudig model voor de fase coherentie. In dit model zijn vier verschillende functies voor de radarreflectie gebruikt: de symmetrische Delta functie (2.6), de symmetrische rechthoekige functie (2.9), de asymmetrische Delta functie (2.12) en de asymmetrische rechthoekige functie (2.13). In het algemeen kan gesteld worden dat een goede positie correctie voor afzonderlijke bomen alleen mogelijk is indien de vorm van de kroon voor elke boom vooraf bekend is. In de praktijk is het mogelijk om een gemiddelde vorm aan te nemen die resulteert in een geoptimaliseerde correctie vergelijking. De resultaten laten zien dat de coherentie zich goed laat voorspellen op basis van veldwaarnemingen en eenvoudige modellen voor de verticale spreiding van de radarreflectie. Er is aangetoond dat een model met horizontale vlakken al een redelijk resultaat heeft.

Hoofdstuk 3 beschrijft een 3D expliciete InSAR-beeld simulatie methode voor bos. De werkwijze kan gebruikt worden bij het toetsen van algorithmen voor boomlaag reconstructie. Het InSAR simulatie model is een uitbreiding van het *water cloud model* [3] met interferometrische fase en coherentie, en met de geometrie van iedere boomkroon. Beeldsimulaties zijn gedaan voor drie waarden van de

extinctie coefficient α : 0.075 m^{-1} , 0.15 m^{-1} en 0.3 m^{-1} . Voor X- en C-band wordt de boomkroon beschreven door een isotroop random medium bestaande uit een groot aantal onafhankelijke reflectoren per resolutie cell (single scattering). Het totale bos wordt beschreven door twee parameters, σ_v en α en door de bosstructuur functie $S(x, y, z)$. De resultaten laten zien dat het model mogelijk niet correct is voor X-band. Voor C-band zijn de aannamen beter en een extinctie coefficient $0.15 < \alpha < 0.3 \text{ m}^{-1}$ lijkt realistisch.

Hoofdstuk 4 introduceert een theorie voor 3D boomkroon reconstructie uit InSAR data. Een statistisch optimale methode wordt behandeld onder de aanname dat het elektrische veld (E_1 en E_2) een complex circulair Gaussische kansdichtheid heeft. Gesimuleerde *templates* van boomvormen worden gebruikt voor het optimaal localiseren van boomkronen in de InSAR data. Daartoe worden twee beeldtransformaties geïntroduceerd. De transformatie $H_{\hat{s}}(i_0, j_0, s)$ gebruikt slechts de radarreflectie om kroon locatie en vorm te schatten. De transformatie $H_{\hat{s}_1, \hat{s}_2, \hat{c}}(i_0, j_0, s)$ daarentegen gebruikt ook nog interferometrische fase en coherentie. De transformatie $H_{\hat{s}}(i_0, j_0, s)$ kan efficiënt geïmplementeerd worden. De transformatie $H_{\hat{s}_1, \hat{s}_2, \hat{c}}(i_0, j_0, s)$ daarentegen moet nog verder onderzocht worden om tot een efficiënte implementatie te komen.

Hoofdstuk 5 gebruikt InSAR beeldsimulatie voor het bestuderen van het effect van de systeemparemeters: baseline lengte, inkijkhoek, thermische ruis en het aantal *looks*. Het resultaat laat zien dat InSAR's onder relatief lage SNR (15 dB) ook nog operationeel gebruikt kunnen worden voor boomkroon reconstructie. Dit betekent dat enige flexibiliteit voor handen is en dat een hogere resolutie, een hogere vlieghoogte, of een lager zendvermogen gebruikt kan worden.

Bibliography

- [1] J.I.H. Askne, P.B.G. Dammert, L.M.H. Ulander, and G. Smith. C-band repeat-pass interferometric SAR observation of the forest. *IEEE Transactions on Geoscience and Remote Sensing*, 35(1):25–35, 1997.
- [2] E. Attema, M.G. Wooding, and J-C. Morin. INDREX-96 Experimenters Handbook, Indonesian Radar Experiment 1996, Final Version. Technical report, ESA-ESTEC, Noordwijk, The Netherlands, June 1996.
- [3] E.P.W. Attema and F.T. Ulaby. Vegetation modeled as a water cloud. *Radio Science*, 13(2):357–364, 1978.
- [4] R. Bamler and P. Hartl. Synthetic Aperture Radar Interferometry. *Inverse Problems*, 14(4):1–54, 1998.
- [5] M. Bertero and P. Boccacci. *Inverse Problems in Imaging*. Institute of Physics Publishing, London, 1998.
- [6] M. Born and E. Wolf. *Principles of Optics: Electromagnetic Theory of Propagation, Interference and Diffraction of Light*. Pergamon, Oxford, 5th edition, 1975.
- [7] P.H. Van Cittert. Kohaerenz-probleme. *Physica*, VI(10):1129–1139, 1939.
- [8] J.C. Curlander and R.N. McDonough. *Synthetic Aperture Radar: Systems and Signal Processing*. John Wiley & Sons, New York, 1991.
- [9] J.C. Dainty. *Laser Speckle and Related Phenomena*. Springer, New York, 1985.
- [10] R.O. Duda and P.E. Hart. *Pattern Classification and Scene Analysis*. Wiley-Interscience, New York, 1973.

-
- [11] N.P. Faller and E.H. Meier. First results with the airborne single-pass DO-SAR interferometer. *IEEE Transactions on Geoscience and Remote Sensing*, 33(5):1230-1237, 1995.
 - [12] A. Freeman. SAR Calibration: An Overview. *IEEE Transactions on Geoscience and Remote Sensing*, 30(6):1107-1121, 1992.
 - [13] G. Galati and R. Crescimboni. *Basic Concepts on Detection, Estimation and Optimum Filtering*. IEE, London, 1991.
 - [14] J.P. Gastellu-Etchegorry. Cloud cover distribution in indonesia. *International Journal of Remote Sensing*, 9(7):1267-1276, 1988.
 - [15] S. Geman and D. Geman. Stochastic relaxation, Gibbs distribution and the Bayesian restoration of images. *IEEE Transactions on Pattern Analysis and Machine Intelligence*, 6:721-741, 1984.
 - [16] W. Goblirsch. *Optimization of Geometric Parameters for Interferometric Surface Model Generation*. PhD thesis, University Zürich, March 1997.
 - [17] J. Goodman. *Statistical Optics*. Wiley-Interscience, New York, 1985.
 - [18] L.C. Graham. Synthetic interferometer radar for topographic mapping. *Proc. IEEE*, 62(6):763-768, 1974.
 - [19] C.W. Groetsch. *Inverse problems in the mathematical sciences*. Vieweg & Sohn Verlagsgesellschaft mbH, Wiesbaden, Germany, 1993.
 - [20] J.O. Hagberg, L.M.H. Ulander, and J. Askne. Repeat-pass SAR interferometry over forested terrain. *IEEE Transactions on Geoscience and Remote Sensing*, 33(2):331-340, 1995.
 - [21] D.H. Hoekman. Measurements of the backscatter and attenuation properties of forest stands at X-, C- and L-band. *Remote Sensing of Environment*, 23:397-416, 1987.
 - [22] A. Ishimaru. *Wave Propagation and Scattering in Random Media*, volume 1: Single Scattering and Transport Theory. Academic Press, New York, 1978.
 - [23] W. Kaplan. *Advanced Calculus*. Addison-Wesley, Reading, Massachusetts, third edition, 1984.

-
- [24] M.N.M. Van Lieshout. Stochastic annealing for nearest-neighbour point processes with application to object recognition. *Advances in Applied Probability*, 26:281–300, 1994.
 - [25] J. Marroquin, S. Mitter, and T. Poggio. Probabilistic solution of ill-posed problems in computational vision. *Journal of the American Statistical Association*, 82:76–89, 1987.
 - [26] D. Massonnet and K.L. Feigl. Radar interferometry and its application to changes in the earth's surface. *Reviews of Geophysics*, 36(4):441–500, 1998.
 - [27] C.J. Oliver. Natural clutter in coherent imaging. *Int. J. Remote Sensing*, 12(2):329–338, 1991.
 - [28] T. Poggio, V. Torre, and C. Koch. Computational vision and regularization theory. *Nature*, 317:314–319, 1985.
 - [29] W.H. Press, S.A. Teukolsky, W.T. Vetterling, and B.P. Flannery. *Numerical Recipes in C: The Art of Scientific Computing*. Cambridge University Press, Cambridge, second edition, 1994.
 - [30] E. Rodriguez and J.M. Martin. Theory and design of interferometric synthetic aperture radars. *IEE Proceedings-F*, 139(2):147–159, 1992.
 - [31] K. Sarabandi. Δk -Radar equivalent of interferometric SAR's: A theoretical study for determination of vegetation height. *IEEE Transactions on Geoscience and Remote Sensing*, 35(5):1267–1276, 1997.
 - [32] K. Sarabandi and Y.C Lin. Simulation of interferometric SAR response to deciduous and coniferous forest stands. In *Proceedings IGARSS'97, 3-8 August 1997, Singapore*, pages 1887–1889.
 - [33] K. Sarabandi and Y.C Lin. Simulation of interferometric SAR response for characterizing the scattering phase center statistics of forest canopies. *IEEE Transactions on Geoscience and Remote Sensing*, 38(1):115–125, 2000.
 - [34] G. Sun and K.J. Ranson. A three-dimensional radar backscatter model of forest canopies. *IEEE Trans. Geosci. Remote Sensing*, 33(2):372–382, 1995.

- [35] R.J.A. Tough, D. Blacknell, and S. Quegan. A statistical description of polarimetric and interferometric synthetic aperture radar data. *Proc. R. Soc. Lond. A*, 449:567-589, 1995.
- [36] R. Touzi and A. Lopes. Statistics of the stokes parameters and of the complex coherence parameters in one-look and multilook speckle fields. *IEEE Trans. Geosci. Remote Sensing*, 34(2):519-531, 1996.
- [37] R. Touzi, A. Lopes, J. Bruniquel, and P.W. Vachon. Coherence estimation for SAR imagery. *IEEE Transactions on Geoscience and Remote Sensing*, 37(1):135-149, 1999.
- [38] R.N. Treuhaft, S.N. Madsen, M. Moghaddam, and J.J. Van Zyl. Vegetation characteristics and underlying topography from interferometric radar. *Radio Science*, 31(6):1449-1485, 1996.
- [39] C. Verekamp and D.H. Hoekman. Interferometric phase difference segmentation using parameterized deformable templates. In *Fifth Annual Conference of the Advanced School for Computing and Imaging*, Heijen, The Netherlands., 15-17 June 1999.
- [40] M.L. Williams, S. Quegan, and D. Blacknell. Distribution of backscattered intensity in the distorted born approximation: Application to C-Band SAR images of woodland. *Waves in Random Media*, 7:643-660, 1997.
- [41] I.H. Woodhouse, J. Van der Sanden, and D.H. Hoekman. Scatterometer observations of seasonal backscatter variation over tropical rain forest. *IEEE Transactions on Geoscience and Remote Sensing*, 37(2):859-861, 1999.
- [42] H.A. Zebker and J. Villasenor. Decorrelation in interferometric radar echoes. *IEEE Transactions on Geoscience and Remote Sensing*, 30(5):950-959, 1992.
- [43] F. Zernike. The concept of degree of coherence and its applications to optical problems. *Physica*, V(8):785-795, 1938.

Acknowledgements

First of all, I thank my co-promotor Dirk Hoekman for giving me the opportunity to conduct this research. Having such a knowledgeable scientist just across the corridor is a luxury. I thank my promoter, Prof. Feddes for giving me the necessary freedom and for showing continuing interest in my research.

Special thanks must go to Mahta Moghaddam for inviting me to NASA/JPL and for teaching me the basics of polarimetric SAR interferometry. Other JPL scientists gave valuable feedback on interferometry. I acknowledge Robert Treuhaft, Paul Siqueira and Scott Hensley. This is also the place to thank the Netherlands Organization for Scientific Research (NWO) for awarding me a two months travel grant.

Iain Woodhouse was an important advisor for my work. Many of the early ideas of scattering from tree crowns were tested on Iain during coffee breaks using the blackboard in room 217. Erik Van Halsema was my second advisor. He taught me aspects of interferometry such as coherence estimation and effects of motion compensation. I also thank him for his continuing interest and for accepting me as a member of the Dutch Interferometry Group.

Dirk Hoekman and I soon realized that we lacked knowledge in the field of pattern recognition theory. Marcel Reinders and Emile Hendriks provided us with the necessary fundamentals. Their later feedback on the results is greatly acknowledged. Marie-Colette van Lieshout and Alfred Stein were always ready to draw from their expertise in the field of stochastic spatial modelling. Gary Smiths and Mark Williams are thanked for valuable discussions on InSAR simulation.

From the Department of Water Resources, I wish to thank Remko Uijlenhoet, Ger de Rooij, Mark Hoffman and George Bier who were always willing to discuss topics far from their own areas of expertise. Particular thanks go to Paul Torfs who provided valuable comments concerning mathematics throughout the 4 years of research. Martin Vissers is thanked for his excellent technical support.

The research described is based on a single experiment the preparation and execution of which were in the hands of many experienced people from ESA/ESTEC, Dornier and other institutions. Special thanks go to Evert Attema, Nick Faller and Mike Wooding for execution of INDREX in 1996. Michael Völker was always ready to answer my many questions about the Dornier SAR system. Essential was also acquisition of ground truth data. I very much value the work of Edwin Keizer, Erik van Valkengoed, Anjo de Jong, Kemal Unggul Prakoso, Ruandha Agung Sugardiman, Muljanto Nugroho and Bambang Suryokusumo. Willie Smits and Tinus de Kam are thanked for logistics and support in Indonesia.

Lieve Erika, bedankt voor het steeds weer aansporen tot het afmaken van dit boekje. Nu jouw boekje nog!

List of publications

D.H. Hoekman, C. Verekamp, 1998. High resolution single-pass interferometric radar observation of tropical rain forest trees. *Proceedings of the Fourth International Workshop on Radar Polarimetry. Progress in Electromagnetics Research Symposium*, 1998, pp. 517-525.

C. Verekamp, D.H. Hoekman, 1998. An inversion algorithm for automated retrieval of tree crown characteristics from high-resolution InSAR data. *Second International Workshop on Retrieval of Bio- and Geo-Physical Parameters from SAR Data for Land Applications*, 21-23 October", 1998, Noordwijk, The Netherlands, ESA-ESTEC.

D.H. Hoekman, C. Verekamp, 1998. High resolution single-pass interferometric radar observation of tropical rain forest trees. *Second International Workshop on Retrieval of Bio- and Geo-Physical Parameters from SAR Data for Land Applications*, 21-23 October", 1998, Noordwijk, The Netherlands, ESA-ESTEC.

C. Verekamp, D.H. Hoekman, 1999. Interferometric phase difference segmentation using Fourier parameterised deformable models. *Fifth Annual Conference of the Advanced School for Computing and Imaging*, 15-17 June, 1999, Heijen, The Netherlands.

C. Verekamp, D.H. Hoekman, 1999. Segmentation of high-resolution across-track InSAR data using Fourier parameterised deformable models. *Int J. Remote Sensing* (accepted).

D.H. Hoekman, C. Verekamp, 2000. High resolution single-pass interferometric radar observation of tropical rain forest trees. *IEEE Trans. on Geosci. Remote Sensing* (accepted).

C. Verekamp, D.H. Hoekman, 2000. Comparison of simulated and measured high-resolution InSAR data of a tropical forest scene. *3rd European Conference on Synthetic Aperture Radar*, 23-25 May 2000, Munich, Germany.

C. Verekamp, D.H. Hoekman, 2000. Validation of an InSAR image simulation method for three-dimensional forest. *IEEE Trans. on Geosci. Remote Sensing* (in preparation).

C. Verekamp, D.H. Hoekman, 2000. Forest canopy reconstruction from interferometric SAR. *Inverse problems* (in preparation).

Curriculum Vitae

Chris Varekamp, born on 19 augustus 1969, Wageningen

- 1988 VWO degree, Wagenings Lyceum
- 1989 Exchange visit to Australia
- 1995 Degree Wageningen University
 Subjects MSc theses: Microwave remote sensing, Geostatistics
- 1995 Consultant, CMG Telecommunications & Utilities, Utrecht
- 1996 Start of doctorate research at Wageningen University
 Thesis subject: Interferometric Synthetic Aperture Radar
- 1999 Research fellowship at Jet Propulsion Laboratory, USA, funded
 by The Netherlands Organization for Scientific Research (NWO)

Cover: Phase difference image of tropical forest in East-Kalimantan. The image is a subset of 2000 azimuth lines by 1400 range pixels taken from track Kal.17A. The image was acquired with the airborne Dornier SAR system during the Indonesian Radar Experiment (INDREX) in 1996.